SECRET

Copy 2
RM L55I27b

RESEARCH MEMORANDUM

TRANSONIC AERODYNAMIC AND TRIM CHARACTERISTICS OF A MULTI-ENGINE DELTA-WING AIRPLANE MODEL

By John M. Swihart and Willard E. Foss, Jr.

Langley Aeronautical Laboratory
Langley Field, Va.

NATIONAL ADVISORY COMMITTEE
FOR AERONAUTICS

WASHINGTON
February 17, 1956

NATIONAL ADVISORY COMMITTEE FOR AERONAUTICS

RESEARCH MEMORANDUM

TRANSONIC AERODYNAMIC AND TRIM CHARACTERISTICS OF A MULTI-ENGINE DELTA-WING AIRPLANE MODEL

By John M. Swihart and Willard E. Foss, Jr.

SUMMARY

An investigation of three models of a delta-wing airplane designed for a long-range subsonic cruise and a supersonic dash has been conducted in the Langley 16-foot transonic tunnel. A two-engine version of the airplane was tested at essentially zero lift and it was found to have a high transonic drag rise. The two four-engine models were designed according to area-rule concepts to have better performance characteristics than the two-engine model. The four-engine delta-wing airplane models were similar in all respects except that one had a plane delta wing with full-span elevons and the other had a cambered delta wing with partial-span elevons. The Mach number range of the investigation was from 0.70 to 1.06 and the Reynolds number range was from 8.5×10^6 to 13.3×10^6 based on wing mean aerodynamic chord. The angle-of-attack range for the four-engine models was varied from about -3° to a value necessary to obtain a lift coefficient of about 0.3. Model trim characteristics were obtained on the four-engine versions by deflecting the elevons from 0° to -2° and -4°. Both four-engine models were tested with four single-engine nacelles and two twin-engine nacelles.

The results of the investigation indicated that the four-engine ~~delta-wing~~ airplane models had considerably lower transonic-drag-rise increments than the two-engine model but did not achieve the low transonic-drag-rise increment of a similar four-engine delta-wing configuration with a nearly parabolic axial distribution of cross-sectional area. The higher drag rise of the four-engine delta-wing airplane models compared with the more idealized four-engine configuration was attributed to an auxiliary horizontal aerodynamic surface in close proximity to the wing and to other dissimilarities including wing incidence of 3°, canopy, increase in wing thickness ratio, landing-gear fairings, afterbody shape, and different distributions of cross-sectional area above and below the wing-chord plane.

The conically cambered-wing models had higher values of maximum lift-drag ratio than the plane-wing models throughout the Mach number range investigated. The cambered-wing twin-engine nacelle configuration had the highest value of maximum lift-drag ratio for Mach numbers below 0.92. For trimmed flight with a static margin 3 percent of the mean aerodynamic chord at a lift coefficient of 0.25 (near cruising lift coefficient), the cambered-wing twin-engine nacelle configuration had highest lift-drag ratio and nearly constant elevon deflection over the Mach number range investigated.

INTRODUCTION

Earlier tests of a two-engine delta-wing airplane model designed for a long-range cruising flight and a supersonic dash indicated a high zero-lift drag rise through the transonic speed range. In an effort to reduce the drag rise of this two-engine airplane model, a four-engine delta-wing configuration (model 1 of ref. 1) was designed based on the concepts of reference 2 to have an axial distribution of cross-sectional area similar to that of a parabolic body of revolution with a fineness ratio of 9. Data from the free-flight test of this configuration indicated a considerably lower zero-lift drag rise than the original two-engine delta-wing airplane model. Further evidence to support the area-distribution concepts for model 1 of reference 1 was obtained when tests of a body of revolution having the same axial distribution of cross-sectional area yielded almost the same value of drag rise (ref. 1). These results led to the design of a four-engine delta-wing airplane model with an area distribution very similar to that of model 1 of reference 1 but incorporating some deviations necessitated by practical aircraft design.

The earlier investigation of the two-engine delta-wing airplane model to determine the zero-lift drag rise was made in the Langley 16-foot transonic tunnel and is reported herein for comparison purposes. Two versions of the redesigned four-engine delta-wing airplane model have been investigated at lifting conditions in the Langley 16-foot transonic tunnel. The investigation of the four-engine delta-wing airplane models was to determine the rise in minimum drag coefficient with Mach number and to evaluate the trim characteristics of several wing and nacelle configurations in the transonic speed range. The effects of nacelles and various aerodynamic surfaces attached to the droppable store (flush mounted beneath the fuselage) on the transonic rise of minimum drag coefficient were also investigated.

The two four-engine delta-wing airplane models were similar in all respects except that one had a plane delta wing with full-span elevons and the other had a cambered delta wing with partial-span elevons. A cambered-wing model was used for the present investigation because of the expected lower values of drag at lifting conditions (refs. 3 and 4) that might be attained in comparison with the plane-wing model. Both the four-engine models were tested with four single-engine nacelles and two twin-engine nacelles, hereafter referred to as "split" nacelles and "Siamese" nacelles, respectively. The Siamese nacelles were considered advantageous from a power-package assessment even though the model with these nacelles had a less favorable cross-sectional area distribution than the model with split nacelles and, therefore, might be subject to higher values of drag rise.

All configurations, the two-engine model and the four-engine models, were tested at an elevon deflection of 0°. The Mach number range for the two-engine model was from 0.80 to 1.06 and the corresponding Reynolds number range based on the wing mean aerodynamic chord was from 12.3×10^6 to 13.3×10^6. The Mach number range for the four-engine models was from 0.70 to 1.06 and the Reynolds number range based on wing mean aerodynamic chord was from 8.5×10^6 to 9.3×10^6. Additional tests were also made at elevon deflections of -2° and -4° for most of the four-engine model configurations in order to determine the model trim characteristics. The angle of attack for the two-engine model was maintained very near to 0° in order to maintain zero lift over the Mach number range. In general, the angle of attack of the four-engine models was varied from about -3° to a value necessary to obtain a lift coefficient of about 0.3.

SYMBOLS

A	cross-sectional area
AR	aspect ratio
B	base area
b	wing span
C_D	drag coefficient, $\frac{D}{q_o S} = C_{D_T} - C_{F_B} - C_{F_I}$
C_{D_T}	balance-measurement drag coefficient
C_{F_B}	base force coefficient, $\frac{P_B B}{S} \cos(\alpha + i)$
C_{F_I}	nacelle internal-force coefficient, $\frac{m(V_o - V_E) - A_E(p_E - p_o)}{q_o S} \cos(\alpha + i)$
C_L	lift coefficient, $L/q_o S$
C_m	pitching-moment coefficient, $M_{0.35c'}/q_o S c'$
C_{m_o}	pitching-moment coefficient for zero lift

[redacted]

c'	mean aerodynamic chord
D	external drag
i	angle between nacelle center line and fuselage reference line
L	lift
l	model length
$M_{0.35c'}$	pitching moment about 0.35c'
M	Mach number
m	mass flow
m'	point mass-flow ratio, $\rho_E V_E / \rho_o V_o$
P	pressure coefficient, $\frac{p_{local} - p_o}{q_o}$
p	static pressure
q	dynamic pressure
R	Reynolds number
S	wing area
V	velocity
X	distance from wing leading edge
x	distance to rear of nose
α	model angle of attack measured from fuselage reference line
δ	deflection angle of elevon, positive down
ρ	mass density

Slope parameters:

$$C_{L_\alpha} = \left(\frac{\partial C_L}{\partial \alpha}\right)_{\delta=0^\circ}$$

[redacted]

$$C_{L_\delta} = \left(\frac{\partial C_L}{\partial \delta}\right)_{\alpha=0^\circ}$$

$$C_{m_\delta} = \left(\frac{\partial C_m}{\partial \delta}\right)_{\alpha=0^\circ}$$

Subscripts:

B	base
E	nacelle exit station
I	internal
max	maximum
o	free stream except in C_{m_o}

MODEL DESCRIPTION

Two-Engine Model

A sketch of the two-engine delta-wing airplane model is shown in figure 1 and dimensions for the model are given in table I. The model was constructed of magnesium and mahogany. The wing had a delta plan form with the leading edge swept back 65° and NACA 65A004 airfoil sections parallel to the plane of symmetry. The fuselage and the droppable store (hereafter referred to as a "pod") were designed to separate on the parting line shown in figure 1. A photograph of the two-engine delta-wing airplane model mounted in the tunnel is shown as figure 2. The nacelles were set at an angle of incidence of -2.13° with respect to the wing.

Figure 3 shows the nacelle configuration with the central spike inlet and table II gives the nacelle and nacelle central spike dimensions.

Four-Engine Models

Fuselage and droppable pod.- A schematic diagram showing model details is presented in figure 4 and additional details of the model geometry are given in table III. The fuselage-pod combination shown in figure 4 is indented for a Mach number of 1.00 in accordance with the area-rule considerations as given in reference 2. The droppable

[redacted]

pod is attached to the undersurface of the fuselage and the pod aerodynamic controls consist of a canard, pod wing, and pod ventral fin.

Plane-wing model.- The plane-wing model had 60° sweep of the wing leading edge, -10° sweep of the wing trailing edge, 3° of incidence, an aspect ratio of 2.1, and incorporated NACA 0004.08-63 airfoil sections. Solid magnesium construction with an overlay of bonded mahogany over the midchord sections was employed on the delta wing which had full-span elevons and provisions for mounting either Siamese or split nacelles.

Cambered-wing model.- The cambered-wing model was similar in all respects including construction material to the plane-wing model except for the leading-edge camber (15 percent of the local semispan, see fig. 5) and the smaller elevon area of the cambered wing. The leading edge of the wing was drooped 2.86 percent of the local semispan to provide a nearly elliptical spanwise loading at the design lift coefficient (0.22) and Mach number (1.414). The elevons on the cambered wing extended to 79.7 percent of the wing semispan. For additional details of the cambered-wing design, see figure 5 and table IV.

Split nacelles.- Four separate nacelles (designated herein as "split nacelles" to denote a single-engine ducting system) were mounted in an identical manner on both the plane or cambered wing. The split-nacelle configuration (fig. 4) consisted of: (a) two inboard pylon-mounted nacelles suspended at 40.30 percent of the wing semispan with the longitudinal axis parallel to the wing chord (fig. 6 and table V), and (b) two outboard nacelles mounted flush on the upper surface of the wing at 64.63 percent of the semispan and at an angle of incidence to the wing chord of -3° (fig. 7 and table VI). All split nacelles were made of magnesium and had the same internal contour (table V).

Siamese nacelles.- The Siamese nacelles (the term "Siamese nacelle" denotes a mated pair of engine ducting systems) were suspended from the lower surface of each wing parallel to the chord plane on a pylon at 45.72 percent of the semispan (fig. 8 and table VII). The same internal contours were maintained for the Siamese nacelle ducting as for the split nacelle.

Photographs showing three-quarter front views of the plane-wing model with split nacelles and the cambered-wing model with Siamese nacelles are given in figure 9. Front views of the same configurations are presented in figure 10. Photographs showing the pod-wing location and the manner in which the pod wing was faired to the main wing are given in figure 11. The tip sections of the faired pod wing are located inside the landing-gear fairings as indicated by the dashed lines on the figure.

[redacted]

TESTS

Tests of a two-engine delta-wing airplane model and two four-engine delta-wing airplane models have been conducted in the Langley 16-foot transonic tunnel. The operational and flow characteristics of the wind tunnel are given in reference 5.

The force tests for the four-engine models were conducted at Mach numbers from 0.70 to 1.06 and at Reynolds numbers from 8.5 to 9.3 $\times 10^6$ (fig. 12). For the two-engine model the angle of attack was kept very close to 0° to maintain zero lift over a Mach number range from 0.80 to 1.06 and at Reynolds numbers from 12.3 to 13.3 $\times 10^6$. In general, the angle of attack of the four-engine model was varied, at a given Mach number, from about -3° to a value necessary to produce a lift coefficient of about 0.3. This lift coefficient was slightly higher than the design transonic cruise lift coefficient of 0.25. The four basic configurations (plane-wing split nacelles, plane-wing Siamese nacelles, cambered-wing split nacelles, and cambered-wing Siamese nacelles) were tested throughout the Mach number range for an elevon deflection of 0°. The plane-wing split-nacelle, cambered-wing split-nacelle, and the cambered-wing Siamese nacelle configurations were also tested at an elevon deflection of -2° and -4°. Additional tests were conducted throughout the Mach number range at an elevon setting of 0° for the plane wing with outboard split nacelles removed and for the plane and cambered wings without nacelles. There was air flow through the ducts for all nacelle-on tests on both the two-engine and the four-engine models. A drag breakdown for the four-engine models was obtained by testing the plane-wing split-nacelle configuration with various pod components removed (canard, pod wing, and pod ventral fin shown in fig. 11(a)). One test was made with the pod wing faired to the main wing for the plane-wing split-nacelle configuration (fig. 11(b)).

Pressure tests to determine base pressure coefficient and nacelle internal-force coefficient were made simultaneously with the force tests for the two-engine airplane model. Pressure tests were made separately from the force tests but throughout the same angle-of-attack and Mach number range for the four-engine models with elevon deflections of 0° and -4°.

METHODS

Instrumentation

The force data for the models tested were obtained from an internally mounted six-component strain-gage balance. Fuselage base-pressure

[redacted]

forces, nacelle base-pressure forces, and nacelle internal forces were determined from pressure measurements. Internal pressures were measured near the exits of both nacelles on the two-engine model and near the exit of one inboard split nacelle and one duct of a Siamese nacelle on the four-engine model. Choked flow was obtained in the nacelles of the four-engine models at Mach numbers above 0.95 by using a ratio of exit area to inlet area of 1.10. This ratio in combination with the external nacelle contour resulted in an annular base on each nacelle. (See fig. 6.)

Data Reduction

An automatic punch-card system was used to reduce the force data to coefficient form. All force data presented in this report have been adjusted for base-pressure forces and nacelle internal forces. Figure 13 shows the variation of pod base-pressure coefficient and nacelle internal-force coefficient with Mach number for the two-engine delta-wing airplane model.

The values of base-force coefficient, internal-force coefficient, and point mass-flow ratio for elevon settings of 0° are presented in figure 14 for the four-engine models as a function of angle of attack for the test Mach numbers. In general, the base and internal forces were about the same at an elevon deflection of -4° as at the setting of 0°. The measured values of base-force coefficient and internal-force coefficient were used to adjust the force data, and the -2° elevon data were obtained from an average of the 0° and -4° elevon data.

No correction has been made for sting tares. At the present time, it is believed such effects would be small.

The angle of attack for the four-engine delta-wing airplane model has been corrected for balance and sting deflections and for a tunnel upflow angularity of 0.4° that was invariant with Mach number.

In addition to the corrections already indicated, the values of drag coefficient presented in this report, other than the basic data (shown in figs. 15 to 19) have been adjusted for tunnel-wall reflected-wave disturbances. This adjustment was made by crossplotting the basic drag data against Mach number and then fairing a curve lower than the basic data in the Mach number range from 1.00 to 1.06 where a maximum drag-coefficient-adjustment value of 0.0015 at a Mach number of 1.04 was employed. This value (0.0015) is based directly on a correlation of free-flight tests of the two-engine delta-wing airplane model and the present data for the two-engine delta-wing airplane model at zero lift. This same adjustment was assumed to apply for the four-engine models and at lifting conditions.

[redacted]

Accuracy

The values presented in the following table indicate the maximum error that may be present, including all errors that were detected throughout the process of recording, reducing, and presenting the data in its final form.

C_L	±0.005
C_D	±0.001
C_m	±0.0005
M	±0.005
α, deg	±0.1
P	±0.005

The repeatability of the aerodynamic coefficients was better than the indicated accuracy. It was found that the drag coefficient, for example, repeated within ±0.0005.

RESULTS

The results of the investigation are presented in figures 15 to 31. Basic aerodynamic characteristics are presented for all of the four-engine delta-wing airplane model configurations tested. The zero-lift drag data for the two-engine delta-wing airplane model are presented in comparison with the four-engine delta-wing airplane-model drag data. The variation of slope parameters with Mach number is generally shown for only the four-engine basic configurations tested. The lift-curve and pitching-moment-curve slopes were obtained from straight lines averaging that portion of the curves between a lift coefficient of 0 and 0.3. All reference to the transonic rise in drag coefficient in the following discussion is for the Mach number range from 0.90 to 1.04. The free-stream-tube area containing the mass flow entering the ducts at $M = 1.0$ has been subtracted from all area diagrams presented. An indication of the data presented in figures 15 to 31 is given in the following table:

	Figure
Basic aerodynamic characteristics (α, C_D, and C_m against C_L)	15 to 19
Drag-rise plots and area diagrams	20 to 22
Effect of wing camber on drag coefficient	23
Effect of camber on drag due to lift at M = 0.90	24
Variation of maximum lift-drag ratio and lift coefficient for maximum lift-drag ratio with Mach number	25
Variation of lift-curve slope with Mach number	26

[redacted]

DISCUSSION

Aerodynamic Characteristics of Models

Variation of minimum drag coefficient with Mach number.- One of the purposes of the present investigation was to determine the transonic drag-rise characteristics of a long-range delta-wing airplane model. Earlier tests of the original version of the airplane, the two-engine delta-wing airplane model conducted in the Langley 16-foot transonic tunnel, indicated a high zero-lift drag rise. Specifically, these tests of the two-engine delta-wing airplane model show a zero-lift transonic drag-rise of 0.0212 (fig. 20(a)). In an effort to reduce the transonic drag rise of this airplane model, an idealized four-engine delta-wing configuration was designed to have an axial cross-sectional area distribution almost the same as that of a parabolic body of revolution having a fineness ratio of 9.0. This attempt at transonic-drag-rise reduction was based on the results of reference 2 which showed that the zero-lift drag rise of a wing-body combination could be reduced by designing the configuration to have a gradual axial increase and decrease in total cross-sectional area and by keeping the maximum cross-sectional area to a minimum. The results of the free-flight test of the four-engine delta-wing configuration (model 1 of ref. 1) indicated a zero-lift drag rise of 0.0100. The validity of area-rule concepts in the design of model 1 of reference 1 was further established by achieving the same drag-rise increment (0.0100) with a body of revolution having an axial cross-sectional area distribution identical with that of model 1. These results led to the present design of the four-engine delta-wing airplane models.

These four-engine models have an area distribution approaching that of model 1 of reference 1 on a total cross-sectional area basis. The nondimensional area progressions of these models are presented in figure 20(b). The difference in nondimensional cross-sectional area between model 1 of reference 1 and the present four-engine delta-wing airplane model with split nacelles is primarily the result of a difference in fineness ratio between the models (9.0 and 8.2, respectively). Some difference is also due to a more rearward location of the maximum cross-sectional area.

A transonic drag rise of 0.0154 was measured for the plane-wing split-nacelle model and 0.0175, for the same wing with Siamese nacelles as shown in figure 20(a). Inspection of the area diagrams (fig. 20(b)) indicates that the split nacelles have the more favorable area distribution and, therefore, these nacelles should have a lower transonic drag rise than the Siamese nacelles. Although the four-engine delta-wing airplane models show an appreciable reduction in drag rise when compared with the two-engine model, they have about 50 percent higher drag rise than model 1 of reference 1. The reason for the failure of the present models to achieve the low (0.0100) drag rise increment of model 1 can be explained by noting the physical differences between the models and the results from the present drag-breakdown tests. The physical differences between the models are as follows:

	Present model	Model 1 of ref. 1
Pod wing	Yes	None
Incidence, deg	3	None
Fineness ratio (equivalent body)	8.2	9.0
Landing-gear fairings	Yes	None
Canopy	Yes	None
Canard	Yes	None
Wing thickness, percent	4.08	3.0
Afterbody shape	Slightly different diameters and slopes	

The four-engine models differed also in their distribution of cross-sectional area in that the present models had an unsymmetrical distribution above and below the wing-chord plane (fig. 20(b)), whereas model 1 had a nearly symmetrical distribution.

The results of drag-breakdown tests for the pod components on the plane-wing split-nacelle configuration (fig. 21(a)) indicate that the pod wing is the chief contributor to the transonic drag rise. It adds an increment in the rise of minimum drag coefficient of 0.0020 and, if based on its own area, the drag rise of the pod wing would have the unreasonably high value of 0.0206. Shadowgraphs taken during the tests indicate a shock formation near the trailing edge of the pod wing that is not present for tests without the pod wing. Fairing the pod wing to the main wing (fig. 21(a)) reduced the rise in minimum drag coefficient by about 0.0010. It can be seen in figure 21(b) that the removal of the pod wing lowers the area diagram slightly in a region of high slope, but the difference in drag from area-rule considerations would be less than 0.0020. The 0.0020 increment in drag coefficient emphasizes the point that, when aerodynamic components are added to a configuration, high local interferences may occur, separation may also occur, and for this particular surface choking of the flow between the pod wing and the main wing may result in added drag.

[redacted]

If the increment in transonic drag rise due to the pod wing (0.0020) is subtracted from the drag rise of the complete configuration (0.0154 for the plane wing with split nacelles), the resulting transonic drag rise would be 0.0134 or 0.0034 higher than that for model 1 of reference 1. An analysis made to evaluate the increment in drag rise due to each of the remaining physical differences between the present four-engine models and model 1 indicated that no large drag-rise increment (none of the magnitude of the pod wing at least) could be expected for any one dissimilarity and, in general, it was found that each increment was within the accuracy of the reference data. Since the differences between the models (other than the pod wing) are such that an increase in drag rise for the present four-engine models would be expected, it is believed that the higher drag rise (compared with that of model 1) would be adequately explained if each dissimilarity increased the drag rise by as small an increment as 0.0005.

In general, the nacelle drag increment shown in figure 22(a) indicated no adverse nacelle interference effects.

In the preceding discussion, the comparisons of the data from the four-engine delta-wing airplane models of the present test with that of reference 1 have been confined to the plane wing. The cambered wing could have been used for the comparisons also since it shows almost the same rise in minimum drag coefficient for a given nacelle installation as the plane wing. (See fig. 20(a).)

Calculations of the zero-lift drag rise for several of the configurations tested using the method of reference 6 were consistently lower than the measured results, often by as much as 50 percent. It is believed that the inability of the method to give accurate predictions is related to the abrupt changes in slope of the area diagrams for the configurations being investigated, and the inability of the method to include the effects of separated flow and choked flow. The method accurately predicted the zero-lift drag rise of model 1 of reference 1, which had a fairly smooth cross-sectional area progression.

Variation of C_D with Mach number at $C_L = 0.25$.- Model 1 of reference 1 and the two-engine delta-wing airplane model were not investigated at lifting conditions. The lift coefficient of 0.25 was chosen for the drag-coefficient data presented in figure 20(a) because it represents the design lift coefficient for transonic cruising flight of the four-engine delta-wing airplane models. At a lift coefficient of 0.25, the effect of the type of nacelle on the transonic-drag-rise increment is the same as that at the minimum drag coefficient; that is, the Siamese nacelles on either plane or cambered wing maintain an increment in drag rise of about 0.0020 over that of the split nacelles. An interesting aspect of the transonic drag rise under lifting conditions is that the plane wing with a given nacelle has a lower drag rise than the same

[redacted]

configuration has at minimum drag coefficient. The cambered wing with a given nacelle installation, however, has a higher drag rise under lifting conditions than that of the same configuration at minimum drag coefficient. The absolute drag-coefficient level is lower for the cambered-wing models at this lift coefficient than for the plane-wing models for the Mach number range investigated.

Effect of camber on drag coefficient.- The benefits of camber in reducing the drag coefficient at lifting conditions are readily shown in figure 23. In this figure, the drag coefficient of the cambered wing has been subtracted from the drag coefficient of the plane wing at a given Mach number for lift coefficients of 0.15, 0.20, and 0.25 and the results plotted against Mach number. It may be noted that, subsonically, camber provides a reduction in drag coefficient of about 0.0040 for either nacelle installation at a lift coefficient of 0.25. As would be expected, the beneficial effect of camber on the drag coefficient decreases with decreasing lift coefficient. At a Mach number of 1.04, the cambered wing still has an advantage over the plane wing but this advantage is reduced at all lift coefficients.

Effect of camber on the drag due to lift at a Mach number of 0.90.- The beneficial effect of camber on the drag coefficient at selected lift coefficients has been shown in figure 23 over the Mach number range. It is of interest to show the effect of camber on the drag due to lift at a Mach number of 0.90, the selected subsonic cruise speed for this design. Shown in figure 24 is the drag coefficient plotted against lift coefficient for the plane and cambered wings with no nacelles, split nacelles, and Siamese nacelles. For comparison purposes, a curve representing the minimum possible induced drag coefficient $\left(\Delta C_D = \frac{C_L^2}{\pi AR}\right)$ is shown passing through the point for zero-lift drag for the plane wing. It is assumed that the zero-lift drag coefficient for the plane wing represents the skin-friction drag for the configuration and that the additional drag coefficient shown for the cambered wing at zero lift is the increment in drag due to twist and camber. These data show that the cambered wing without nacelles has almost the minimum possible value of induced drag coefficient. The data of reference 4 for a cambered delta wing of aspect ratio 2 indicates this same result up to the design lift coefficient of the wing.

There is an increase of about 22 percent over the minimum possible value of induced drag coefficient for both nacelle configurations at a lift coefficient of 0.25. This increase in the drag due to lift is probably the result of the nacelles and fuselage causing distortion of the design elliptical span load distribution on the wing. Reference 7 indicates that there should be no decrease in the drag due to lift when the test Reynolds number is 10×10^6 or greater. If the plane-wing zero-lift drag coefficient (0.0133) is

[redacted]

converted to the skin-friction drag coefficient by the ratio of model wing area to wetted area, the skin-friction drag coefficient is 0.0033. The value of the skin-friction drag coefficient for the flat plate at $M = 0.90$ and $R = 10 \times 10^6$ is 0.0028 (ref. 8). This low value of skin-friction drag coefficient thus precludes any large interferences that might cause separation drag. Since the model with no nacelles has almost the minimum possible value of drag due to lift, it would not be expected that an increase in Reynolds number would result in a decrease in the drag due to lift.

Variation of $(L/D)_{max}$ and $C_{L_{(L/D)_{max}}}$ with Mach number.- The variation of $(L/D)_{max}$ with Mach number (fig. 25) shows that the cambered wing with either split or Siamese nacelle has a higher value of $(L/D)_{max}$ than the plane wing with either nacelle. Below a Mach number of about 0.92, the Siamese nacelles on either wing have a slightly higher $(L/D)_{max}$ than the split nacelles on either wing. The highest value of $(L/D)_{max}$ (that is, 10.7) for the principal configurations tested occurred for the cambered-wing Siamese nacelle configuration at a Mach number of 0.70. For Mach numbers above 0.97, the cambered-wing split-nacelle configuration has higher values of $(L/D)_{max}$ than the cambered wing with Siamese nacelles. Below a Mach number of 0.95, the cambered-wing nacelle configurations attain $(L/D)_{max}$ at a C_L of about 0.24 (fig. 25), whereas the plane-wing nacelle configurations attain their $(L/D)_{max}$ at a C_L of about 0.20. The added advantage of the cambered wing is also realized in noting that its $(L/D)_{max}$ occurs at nearly the cruising lift coefficient of the aircraft.

Variation of C_{L_α} with Mach number.- In general, the variation of the lift-curve slope C_{L_α} with Mach number is about the same for the four principal four-engine configurations tested (fig. 26). The lift-curve slope C_{L_α} varies from about 0.045 subsonically to about 0.057 near Mach number 1.0. For Mach numbers up to 0.96, the split nacelles have a slightly higher value of C_{L_α} than the Siamese nacelles on either wing.

Variation of C_{m_o}, $\partial C_m/\partial C_L$, and $C_{m_{C_L=0.25}}$ with Mach number.- The zero-lift pitching-moment coefficient C_{m_o} generally shows a small negative increase with Mach number up to $M = 0.95$ (fig. 27). For Mach numbers higher than 0.95 and up to $M = 1.0$, the split nacelles on either wing produce higher negative values of C_{m_o}. The Siamese nacelles on either wing, however, have lower negative values of C_{m_o} for Mach numbers above 0.95. The different trend in the variation of C_{m_o} with Mach

number for the two types of nacelles is shown in a trim analysis in a subsequent section of this paper to have an important bearing on nacelle selection.

The variation of $\partial C_m/\partial C_L$ with Mach number (fig. 28) indicates that the four principal four-engine configurations tested are longitudinally unstable about the 35-percent mean aerodynamic chord up to a Mach number of about 0.95. Beyond this Mach number, the configurations become stable, with the Siamese nacelle configuration indicating the greatest degree of stability above $M = 0.98$. Both the split and Siamese nacelles produce a destabilizing effect since the configurations without nacelles are stable at practically all Mach numbers.

The pitching-moment coefficient at $\delta = 0^\circ$ (fig. 29) is approximately zero for Mach numbers below 0.80 and increases negatively from $M = 0.80$ to $M = 1.04$ for all four-engine configurations. Elevon deflections of -2° and -4° increase the pitching moment at all Mach numbers for all configurations. At $M = 0.90$, approximately -1° of elevon deflection would be required to trim about the 0.35c' for the split-nacelle configurations.

Effect of Elevon Deflection on Aerodynamic Characteristics of the Four-Engine Model

Variation of C_{L_δ} and C_{m_δ} with Mach number.- In figure 30 the plane-wing split-nacelle configuration shows higher lift effectiveness than the cambered-wing split-nacelle configuration. This increase in lift effectiveness parameter is attributed to the larger elevon area on the plane wing. The cambered-wing Siamese nacelle configuration has the lowest value of lift effectiveness parameter up to a Mach number of 0.95 but the parameter does not decrease for this configuration until a Mach number of 0.97, whereas the plane- and cambered-wing models with split nacelles show a decrease in the parameter above 0.95. This earlier loss in lift effectiveness for the models with split nacelles may be associated with shocks near the base of the outboard split nacelle.

The plane-wing split-nacelle configuration has the largest value of pitching-moment effectiveness parameter up to a Mach number of 0.975. The pitching-moment effectiveness parameter follows the same trends with Mach number as does the lift effectiveness parameter, the cambered-wing Siamese nacelle configuration having the largest values above a Mach number of 0.975. Theoretical considerations would indicate that the maximum value of these parameters would occur at a Mach number of 1.0 but the data indicate that, for configurations where shocks may be located on part of the elevons, the effectiveness of the elevons will decrease at Mach numbers of less than 1.0.

Effect of Mach number on elevon angle, angle of attack, drag coefficient, and lift-drag ratio at trim.- The trim analysis presented in figure 31 for three of the four-engine configurations tested is based on a constant 3-percent-c' static margin and a lift coefficient of 0.25.

At Mach numbers above 0.90, the elevon angle required to trim the cambered- and plane-wing models with split nacelles changed rapidly until an elevon angle of about -3.5° was needed at a Mach number of 1.00. The cambered-wing Siamese-nacelle configuration, however, required a relatively small change in elevon angle for trim over the Mach number range. It was noted previously that the zero-lift pitching moment for the Siamese nacelle configurations became less negative at Mach numbers above 0.90. This decrease in C_{m_0} requires a smaller elevon deflection to trim the cambered-wing Siamese nacelle configuration.

The angle-of-attack variation with Mach number at trim is about 1° for all configurations. The cambered-wing models, however, require a higher angle of attack to trim than the plane-wing models.

It was noted in the discussion of the drag coefficient at a lift coefficient of 0.25 that the drag rise was 0.002 greater for the Siamese nacelles than for the split nacelles. At trim, however, the cambered-wing Siamese nacelle configuration has the lowest value of drag coefficient at all Mach numbers because, as indicated previously, this configuration requires less elevon deflection for trimmed flight. The drag-coefficient data presented in figure 31 were obtained by crossplotting the test data.

The lift-drag ratio at trim for the cambered-wing model with Siamese nacelles reflects the lower drag coefficient for this configuration and is generally higher over the Mach number range than that of the other models.

CONCLUSIONS

An investigation of a two-engine delta-wing airplane model with no fuselage indentation and of two four-engine delta-wing airplane models (the design of which was based on area-rule concepts) in the Langley 16-foot transonic tunnel has indicated the following conclusions:

1. The four-engine delta-wing airplane models with favorable axial distributions of cross-sectional area had considerably lower transonic drag-rise increments than the two-engine delta-wing airplane model.

2. The four-engine delta-wing airplane models had cross-sectional area distributions similar to an idealized four-engine delta-wing configuration with a nearly parabolic distribution of cross-sectional area

but did not have the low minimum drag rise of the latter because of an auxiliary pod surface in close proximity to the wing and other dissimilarities including wing incidence of 3°, canopy, increase in wing thickness, landing-gear fairings, afterbody shape, and area distributions above and below the wing-chord plane.

3. The cambered-wing models had higher values of maximum lift-drag ratio than the plane-wing models throughout the Mach number range. For Mach numbers up to 0.92, the cambered-wing Siamese nacelle configuration had slightly higher values of maximum lift-drag ratio than the cambered-wing split-nacelle configuration.

4. The cambered-wing models had lower drag coefficients than the plane-wing models at lift coefficients from 0.15 to 0.25 throughout the test Mach number range.

5. The cambered-wing model with no nacelles has nearly the minimum possible value of induced drag coefficient at a Mach number of 0.90 and there is only a small increase in the drag due to lift when the nacelles are added. The data indicate that there will be no reduction in drag due to lift when the Reynolds number is increased above the test value of approximately 10×10^{6}.

6. For trimmed flight with a 3-percent static margin and a lift coefficient of 0.25 (near the design cruising lift coefficient), the cambered-wing Siamese nacelle configuration had highest values of lift-drag ratio and nearly constant elevon deflection throughout the Mach number range tested.

Langley Aeronautical Laboratory,
National Advisory Committee for Aeronautics,
Langley Field, Va., September 15, 1955.

[redacted]

REFERENCES

1. Hopko, Russell N., Piland, Robert O., and Hall, James R.: Drag Measurements at Low Lift of a Four-Nacelle Airplane Configuration Having a Longitudinal Distribution of Cross-Sectional Area Conducive to Low Transonic Drag Rise. NACA RM L53E29, 1953.

2. Whitcomb, Richard T.: A Study of the Zero-Lift Drag-Rise Characteristics of Wing-Body Combinations Near the Speed of Sound. NACA RM L52H08, 1952.

3. Jones, Robert T.: Estimated Lift-Drag Ratios at Supersonic Speed. NACA TN 1350, 1947.

4. Hall, Charles F.: Lift, Drag, and Pitching Moment of Low-Aspect-Ratio Wings at Subsonic and Supersonic Speeds. NACA RM A53A30, 1953.

5. Ward, Vernon G., Whitcomb, Charles F., and Pearson, Merwin D.: Air-Flow and Power Characteristics of the Langley 16-Foot Transonic Tunnel With Slotted Test Section. NACA RM L52E01, 1952.

6. Nelson, Robert L., and Stoney, William E., Jr.: Pressure Drag of Bodies at Mach Numbers up to 2.0. NACA RM L53I22c, 1953.

7. Osborne, Robert S., and Kelly, Thomas C.: A Note on the Drag Due to Lift of Delta Wings at Mach Numbers up to 2.0. NACA RM L53A16a, 1953.

8. Van Driest, E. R.: Turbulent Boundary Layer in Compressible Fluids. Jour. Aero. Sci., vol. 18, no. 3, Mar. 1951, pp. 145-160, 216.

[redacted]

TABLE I.- DIMENSIONS OF TWO-ENGINE DELTA-WING AIRPLANE MODEL

Wing:	
Area, sq in.	1,728
Span, in.	56.721
Root chord, in.	60.874
Length of M.A.C., in.	40.583
Airfoil section (parallel to plane of symmetry)	NACA 65A004
Sweepback leading edge, deg	65
Dihedral	-2° 27'
Incidence, deg	0
Aspect ratio	1.86
Fuselage:	
Overall length, in.	80.00
Distance from nose of fuselage to leading edge of wing root chord, in.	12.825
Maximum width, in.	5.980
Pod:	
Overall length, in.	90.162
Distance from pod nose to leading edge of wing root chord, in.	21.025
Maximum width, in.	6.000
Nacelles:	
Overall length, in.	42.621
Exit diameter, in.	3.252
Distance from airplane center line to nacelle center line, in.	16.350
Vertical tail:	
Total area, sq in.	125.271
Span, in.	13.245
Root chord, in.	18.916
Airfoil section (parallel to root chord)	NACA 65A005
Sweepback leading edge, deg	55
Pod tails:	
Total area (one fin), sq in.	70.848
Semispan, in.	9.600
Root chord, in.	9.840
Taper ratio	0.500
Airfoil section (parallel to root chord)	NACA 65A005
Sweepback leading edge, deg	52
Angle between tails, deg	120

[redacted]

TABLE II.- NACELLE AND NACELLE-SPIKE ORDINATES FOR TWO-ENGINE DELTA-WING AIRPLANE MODEL (SEE FIG. 3)

Nacelle station	Open nacelle					
	Radius A	Radius B	Dimension C	Dimension D	Dimension E	Internal radius
-6.000	-----	-----	-----	-----	-----	-----
-2.440	-----	-----	-----	-----	-----	-----
-.621	-----	-----	-----	-----	-----	-----
.000	-----	-----	-----	-----	-----	-----
.950	1.730	0.135	3.460	-----	-----	1.700
2.000	1.895	.505	3.875	-----	-----	1.829
5.000	2.265	1.135	4.870	-----	-----	1.969
8.000	2.485	1.595	5.555	2.485	-----	2.054
11.000	2.590	1.915	5.980	2.590	-----	2.113
13.300	2.600	2.055	6.130	2.600	-----	2.113
16.000	2.600	2.125	6.230	2.600	-----	2.113
19.000	2.600	2.103	6.200	2.600	2.600	2.113
22.000	2.600	2.000	6.100	2.600	2.600	2.113
25.000	2.580	1.849	5.913	2.580	2.580	2.066
28.000	2.520	1.655	5.640	2.520	2.520	1.989
31.000	2.430	1.410	5.273	2.430	2.430	1.911
34.000	2.265	1.130	4.815	2.265	2.265	1.833
37.000	2.055	.840	4.270	1.965	1.965	1.756
40.000	1.780	.530	3.628	1.305	1.305	1.678
42.000	1.562	-----	3.125	.620	.620	1.626

Nacelle spike			
Distance G	Ordinate H	Distance K	Ordinate L
0	0	0	0
2.12	.775	1.00	.22
2.62	.890	2.00	.50
3.12	.945	3.00	.69
3.62	.960	4.00	.82
4.12	.950	5.00	.89
4.62	.925	5.40	.90
5.00	.900		

[redacted]

TABLE III.- FOUR-ENGINE DELTA-WING AIRPLANE MODEL DIMENSIONAL DATA

I. Fuselage:

Overall length, in.	69.60
Maximum width, pod included, in.	4.84
Maximum height, pod included, in.	8.86
Fuselage base area, sq in.	7.62

II. Aerodynamic surfaces:

(a) Dimensions for main surfaces and pod surfaces:

Dimension, unit	Main surfaces		Pod surfaces		
	Wing[1]	Vertical tail	Wing	Canard	Tail
Span, in.	45.49	10.58	14.16	7.12	8.53
Root chord, in.	43.40	10.80	13.51	6.79	8.53
c', in.	28.94	----------	---------	---------	---------
Area, total, sq in.	987.26	80.00	95.67	24.18	51.05
Area, exposed, sq in.	----------	----------	68.52	9.57	---------
NACA airfoil section:					
Root to 3.767	0003.46-64.069	0005-64	0004.5-64	0004.5-64	0004.5-64
3.767 to tip	0004.08-63	0005-64	0004.5-64	0004.5-64	0004.5-64
Leading-edge sweep, deg	60	50	60	60	60
Trailing-edge sweep, deg	-10	----------	-10	-10	---------
Aspect ratio	2.10	(Geometric) 1.40	2.10	2.10	1.43
Taper ratio	0	0.4	0	0	0.40
Incidence, deg	3	----------	0	0	---------
Dihedral, deg	0	----------	0	0	---------
Twist, deg	0	0	0	0	0

[1]For plane or cambered wing.

TABLE III.- FOUR-ENGINE DELTA-WING AIRPLANE MODEL DIMENSIONAL DATA - Concluded

II. Aerodynamic surfaces - Concluded:

	Plane	Cambered
(b) Elevons:		
Area, sq in.	79.01	67.60
Span, in.	19.41	14.80
Root chord, in.	5.79	5.79
Root chord location, percent b/2	14.65	14.65
Tip chord, in.	0	3.26
Tip chord location, percent b/2	100	79.70

III. Nacelles (Areas and diameters given are for one duct.):

Overall length, in.	18.667
Inlet diameter, in.	1.800
Inlet area, total, sq in.	2.544
Spike diameter, nacelle station 0, in.	0.934
Spike area, nacelle station 0, sq in.	0.684
Spike cone angle, deg	50
Inlet area, net, sq in.	1.860
Exit internal diameter, in.	1.614
Exit internal area, sq in.	2.046

	Inboard split	Outboard split	Siamese
Spanwise location, percent b/2	40.300	64.630	45.724
Spanwise location, in.	9.167	14.700	10.400
Location of inlet from nose, in.	23.864	39.576	29.592
Angle between chord plane and center line of nacelle	0	-3	0
Maximum nacelle cross-sectional area, sq in.	6.08	6.08	13.60

TABLE IV.- CAMBERED WING GEOMETRY (SEE FIG. 5)

[All letter dimensions are defined in fig. 5]

(a) Coordinates of mean chord line.

Nondimensional coordinates		Typical span station Y = 12.000 in.	
X/Y	Z/Y	X, in.	Z, in.
0	0.0286	0	0.343
.0175	.0231	.210	.277
.0353	.0196	.424	.235
.0536	.0167	.643	.200
.0722	.0141	.866	.169
.0911	.0119	1.094	.142
.1106	.0098	1.327	.118
.1304	.0080	1.565	.096
.1506	.0063	1.807	.076
.1713	.0049	2.056	.059
.1924	.0036	2.309	.043
.2140	.0024	2.569	.029
.2361	.0014	2.834	.017
.2588	.0007	3.106	.008
.2819	.0002	3.384	.002
.3056	0	3.668	0

(b) Coordinates of airfoil section.

Chordwise airfoil ordinates		Typical span station Y = 12.000 in.		
Percent line[1]	Nondimensional ordinate	A, in.	B, in.	Ordinate, in.
0	0	0		0
.156	.236	.032		.048
.313	.332	.064		.068
.625	.466	.128		.096
.938	.567	.192		.116
1.250	.651	.256		.134
2.500	.902	.513		.185
3.750	1.090	.769		.224
5.000	1.230	1.025		.252
7.500	1.454	1.538		.298
10.000	1.620	2.051		.332
15.000	1.841	3.076		.378
20.000	1.965		4.101	.403
25.000	2.024		5.126	.415
30.000	2.040		6.151	.418
35.000	2.027		7.177	.416
40.000	1.988		8.202	.408
45.000	1.924		9.227	.395
50.000	1.839		10.252	.377
55.000	1.731		11.277	.355
60.000	1.604		12.303	.329
65.000	1.458		13.328	.299
70.000	1.295		14.353	.266
75.000	1.117		15.378	.229
80.000	.924		16.404	.189
85.000	.719		17.429	.147
90.000	.502		18.454	.103
95.000	.276		19.479	.057
100.000	0		20.504	0
L.E. radius	.183			.038
C_B			20.504	
C_A		20.507		

[1]This column is in percent I forward of the point of tangency and percent T aft of this point.

TABLE V.- DIMENSIONS FOR INBOARD SPLIT NACELLE (SEE FIG. 6)

[All dimensions are in inches; all letter dimensions are defined in figure 6]

(a)

Nacelle ordinates						
W	Station					
	2.667	5.333	8.000	10.667	14.667	17.333
	U	U	U	U	U	U
0	1.255	1.267	1.267	1.267	1.267	1.233
.100	1.253	1.262	1.262	1.267	1.267	1.217
.200	1.240	1.257	1.257	1.260	1.260	1.207
.400	1.200	1.240	1.248	1.245	1.235	1.160
.500	1.167	1.222	1.237	1.233	1.217	1.123
.700	1.085	1.170	1.202	1.203	1.160	1.017
.800	1.010	1.137	1.177	1.182	1.123	.948
.900	.937	1.095	1.152	1.153	1.077	.858
1.000	.838	1.043	1.113	1.115	1.018	.743
1.100	.708	.978	1.072	1.070	.947	.592
1.200	.530	.893	1.017	1.012	.848	.337
1.248	-----	-----	-----	-----	-----	0
1.300	.212	.780	.945	.932	.718	
1.320	0	-----	-----	-----	-----	
1.400		.633	.850	.835	.543	
1.500		.368	.713	.693	0	
1.545		0	-----	-----		
1.600			.478	.478		
1.667			0	-----		
1.675				0		

(b)

Nacelle radii		
Station	Radius H	Radius J
0	0.920	0.900
.125		.932
.250		.955
.500		.982
.667	1.067	
.750		.992
1.000		.998
1.250		1.000
1.333	1.167	
2.667	1.255	
4.000	1.267	
16.000	1.267	1.000
17.333	1.233	.915
18.667	1.040	.807

(c)

Nacelle spike radii	
Station	Radius
-1.000	0
-.500	.233
0	.467
.500	.563
1.000	.532
1.500	.449
2.000	.375
2.500	.375
2.750	.375
3.500	.352
4.000	.313
4.500	.235
5.000	.100
5.250	0

[redacted]

TABLE VI.- DIMENSIONS FOR OUTBOARD SPLIT NACELLE (SEE FIG. 7)

Section A-A															
Station 2.667		Station 4.000		Station 5.333		Station 6.667		Station 8.000		Station 9.333		Station 10.667		Station 12.000	
Dimension		Dimension		Dimension		Dimension		Dimension		Dimension		Dimension		Dimension	
B	C	B	C	B	C	B	C	B	C	B	C	B	C	B	C
.219	1.241	.221	1.254	.221	1.255	.222	1.257	223	1.261	223	1.264	.223	1.264	.223	1.264
.436	1.199	.441	1.213	.445	1.223	.448	1.231	.452	1.242	.454	1.248	457	1.255	.457	1.255
.645	1.117	603	1.144	675	1.168	.685	1.187	.695	1.205	.705	1.221	.715	1.239	.715	1.239
.840	1.001	.879	1.047	912	1.087	.939	1.119	963	1.147	987	1.176	1.009	1.203	1.009	1.203
1.017	.853	1.088	.913	1.149	.964	1.196	1.003	1.243	1.043	1.289	1.081	1.335	1.120	1.335	1.120
1.157	.667	1.257	.726	1.339	.773	1.403	.810	1.469	.848	1.535	.928	1.601	925		
1.256	457	1.364	.497	1.453	.529	1.526	555	1.599	.582	1.674	.609	1.745	.635		
1.317	.232	1.423	.251	1.517	.267	1.595	.281	1.673	.295	1.751	.309	1.829	323		
1.337	0	1.445	0	1.541	0	1.619	0	1.699	0	1.778	0	1.857	0		

Station	Radius A
0	.920
1.333	1.180
2.667	1.259
4.000	1.267
5.333	
6.667	
8.000	
9.333	
10.667	
12.000	
13.333	
14.667	
16.000	1.267
17.333	1.220
18.667	1.033

Section B-B			
Station 13.333			
Dimension			
D	E	F	G
1.166	673	1.166	673
1.161	.974	1.165	.978
1.113	1.327		

Section C-C		
Station 14.667		
Dimension		
H	J	K
0		
.067		
.133		
.200		
267		
.333		
.400		
.467		
.533		
600		
.667		
.733		
.800		
.867		
.933	.840	.903
1.000	1.045	1.051
1.067	1.464	1.064

Section D-D					
Station 17.333					
Dimension					
L	M	N	P	Q	R
.907	1.669	.907	1.641	.428	1.142

Note All letter dimensions defined on figure 7.

TABLE VII.- DIMENSIONS FOR SIAMESE NACELLE AND PYLON FAIRING (SEE FIG. 8)

All dimensions are in inches

(a) Nacelle fairing geometry.[1]

Nacelle station	Distance			Radius			
	A	B	C	D	E	F	G
-3.333	0	0	0	-------	-------	-----	-----
-2.000	.243	.191	.243	-------	-------	-----	-----
-1.333	.364	.287	.364	0.083	0.083	0.047	0.047
-1.000	.425	.335	.425	.270	.270	.163	.163
-.333	.546	.430	.546	.690	.690	.453	.453
0	.607	.478	.605	.920	.920	.637	.635
1.333	.798	.627	.782	1.167	1.167	.847	.848
4.000	1.072	.733	.857	Nacelle	Nacelle	2.135	.322
8.000	1.252	.733	.857	contour	contour	-----	.222
12.000	1.267	-----	.827	-------	-------	-----	.178
15.333	1.243	-----	.725	-------	-------	.807	.133
16.000	.957	-----	.445	-------	-------	.550	.090
18.667	.473	-----	0	-------	-------	.097	.077
19.000	.407	-----	-.080	-------	-------	-----	-----
19.658	.270	-----	-.270	-------	-------	-----	-----

(b) Ordinates of the faired pylon at several nacelle stations, measured in a plane perpendicular to the nacelle center line.

Distance up from nacelle center line	Nacelle station									
	16.667	17.333	18.000	18.667	19.333	19.658	20.000	20.667	21.333	22.000	24.000
0.167	-------	0.063	0.038	0.018	-------	-----	-----	-----	-----	-----	-------
.333	-------	.088	.060	.037	-------	0.007	-----	-----	-----	-----	-------
.500	-------	.117	.085	.058	-------	.023	-----	-----	-----	-----	-------
.667	-------	.145	.112	.083	-------	.045	0.017	-----	-----	-----	-------
.833	-------	.177	.140	.110	-------	.065	.038	-----	-----	-----	-------
1.000	-------	.208	.172	.138	-------	.092	.062	0.015	-----	-----	-------
1.167	-------	-----	.200	.167	-------	.120	.090	.043	-----	-----	-------
1.333	-------	-----	-----	.197	-------	.148	.122	.073	0.027	-----	-------
1.500	-------	-----	-----	-----	-------	.178	.153	.110	.063	0.013	
1.667	-------	-----	-----	-----	-------	.210	.187	.147	.102	.052	-------
1.833						-----	.223	-----	.142	.093	-------

[1]H, J, W, and U dimensions same as those for the split nacelle (see table 3). All letter dimensions are defined in figure 8.

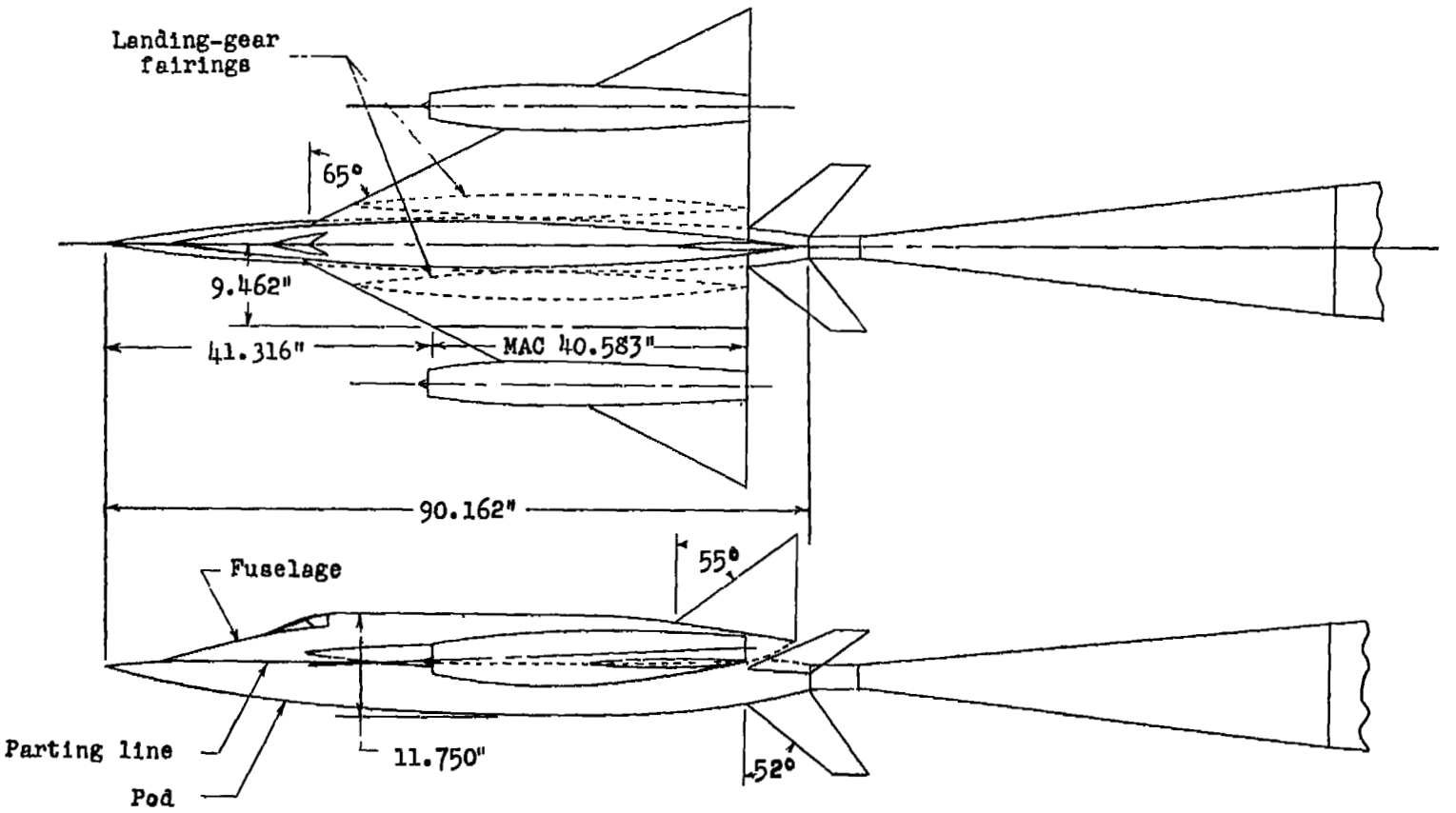

Figure 1.- Sketch of two-engine delta-wing airplane model and wind-tunnel sting assembly. See table I for additional dimensions.

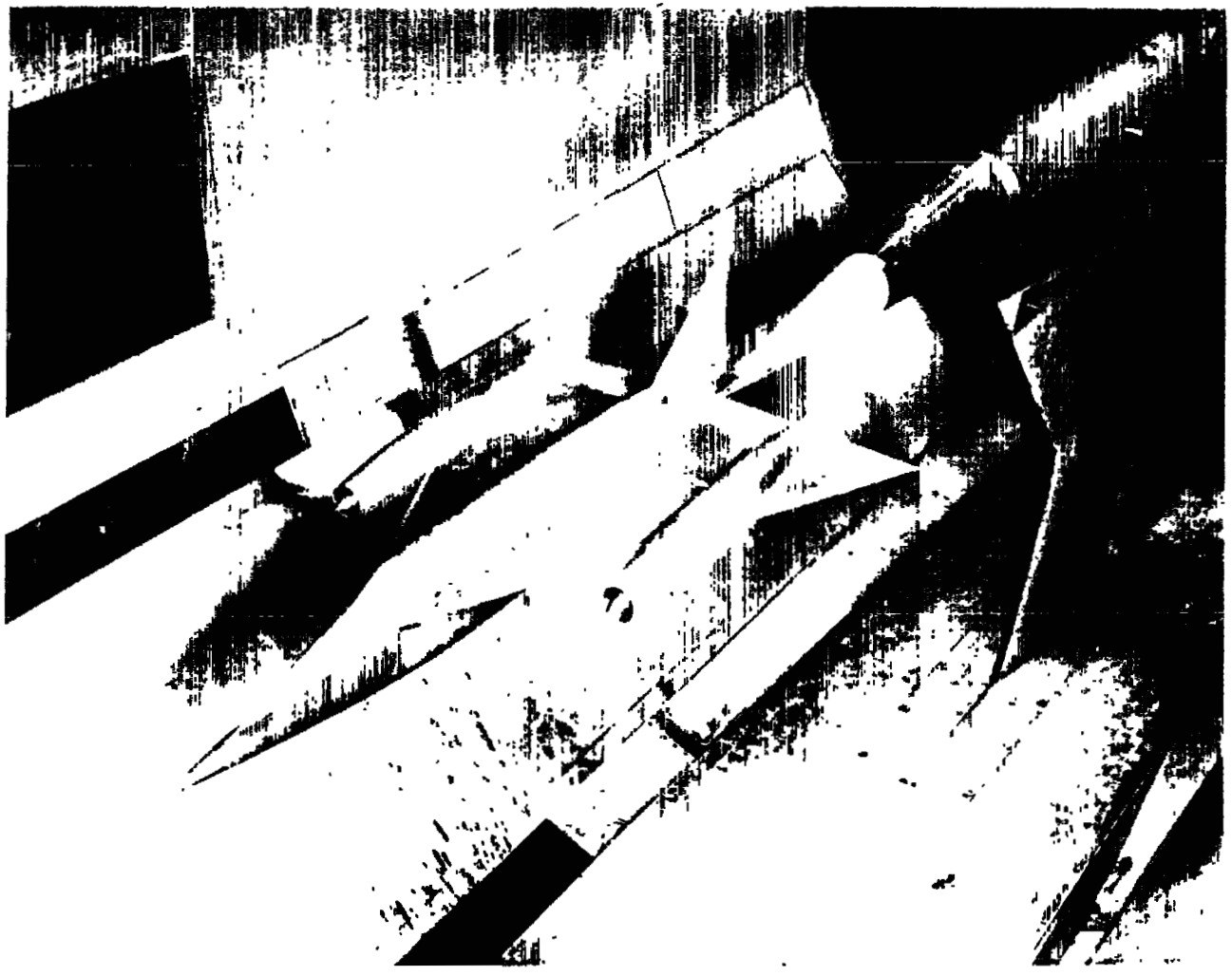

L-78361

Figure 2.- Three-quarter front view of the two-engine delta-wing airplane model mounted in the Langley 16-foot transonic tunnel.

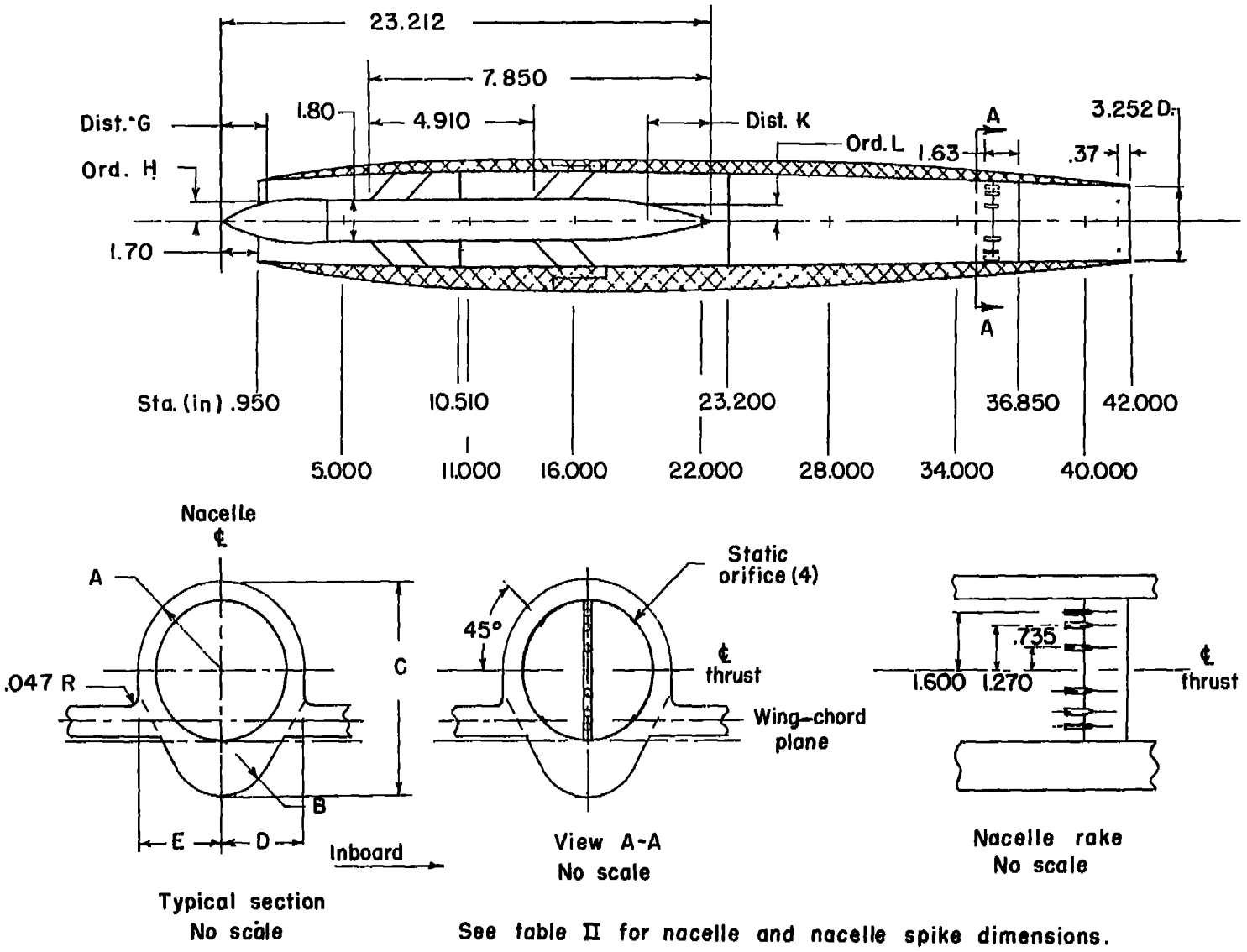

Figure 3.- Nacelle and nacelle spike configuration for the two-engine delta-wing airplane model.

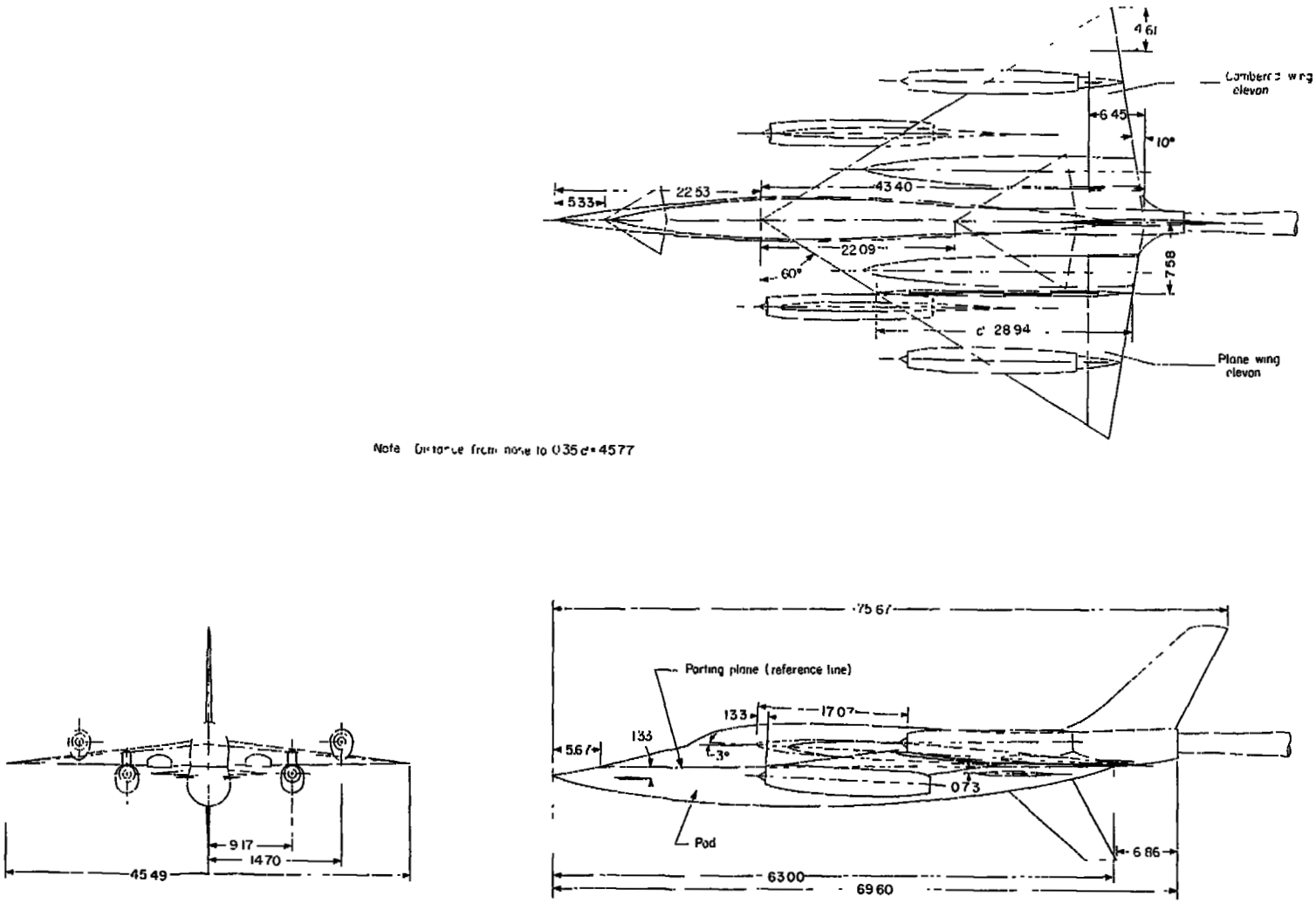

Figure 4.- Four-engine delta-wing airplane model with split nacelles. See table III for additional information. (All dimensions are in inches.)

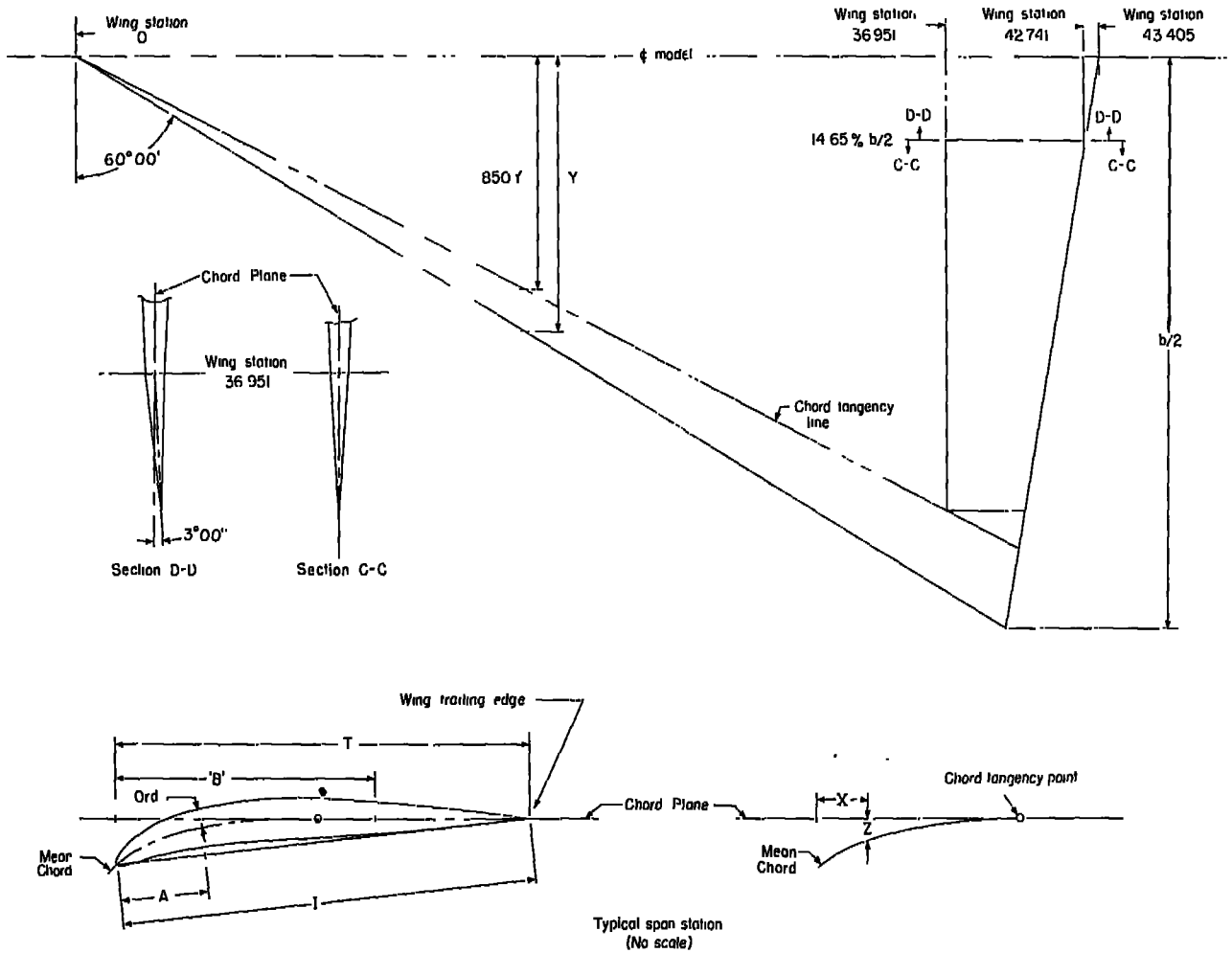

Figure 5.- Details of the cambered-wing construction for the four-engine delta-wing airplane model. See table IV for dimensions not given on the figure. (All dimensions are in inches.)

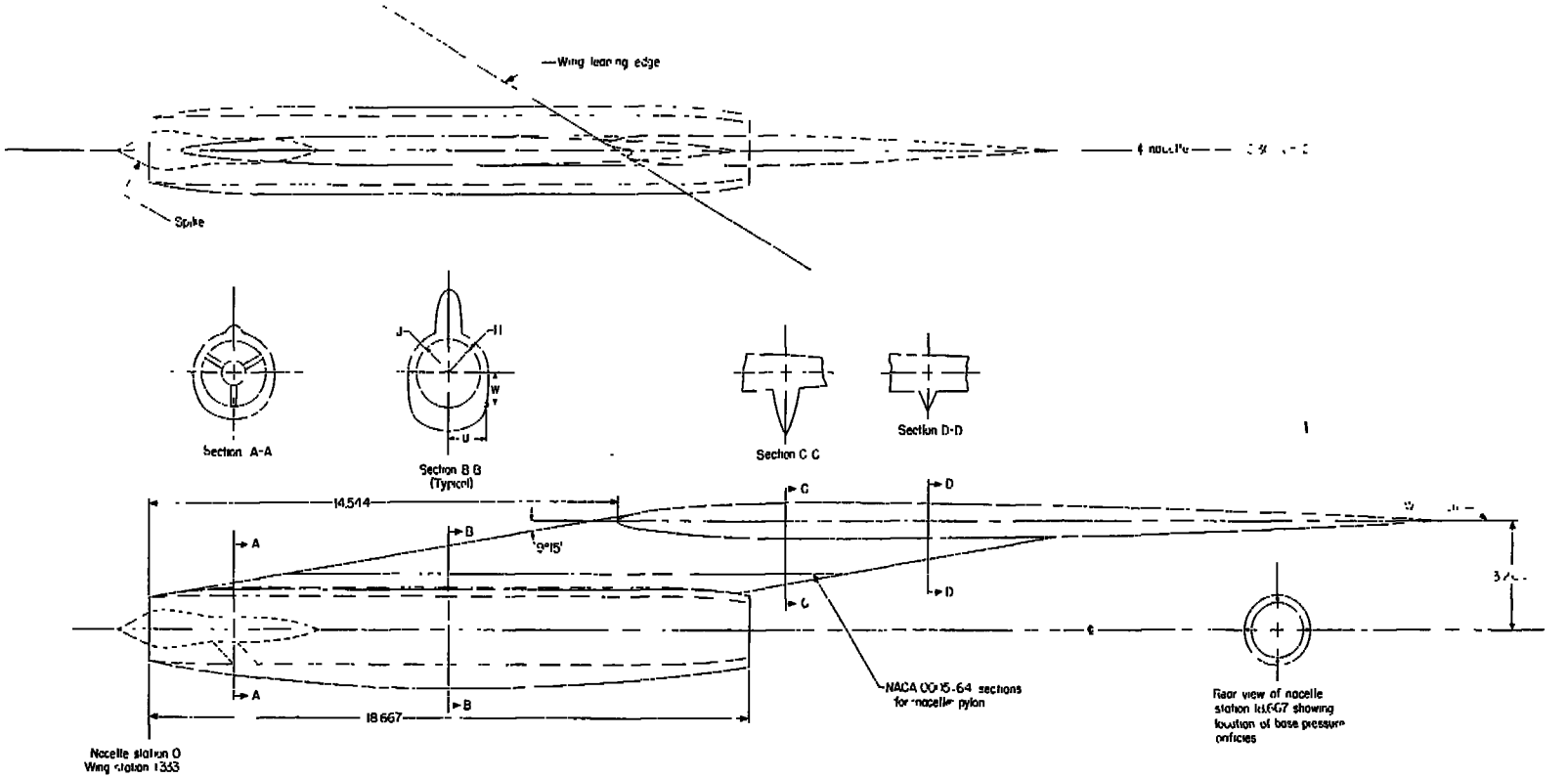

Figure 6.- Geometry of inboard split nacelle and nacelle strut. See table V for dimensions not given on the figure. (All dimensions are in inches.)

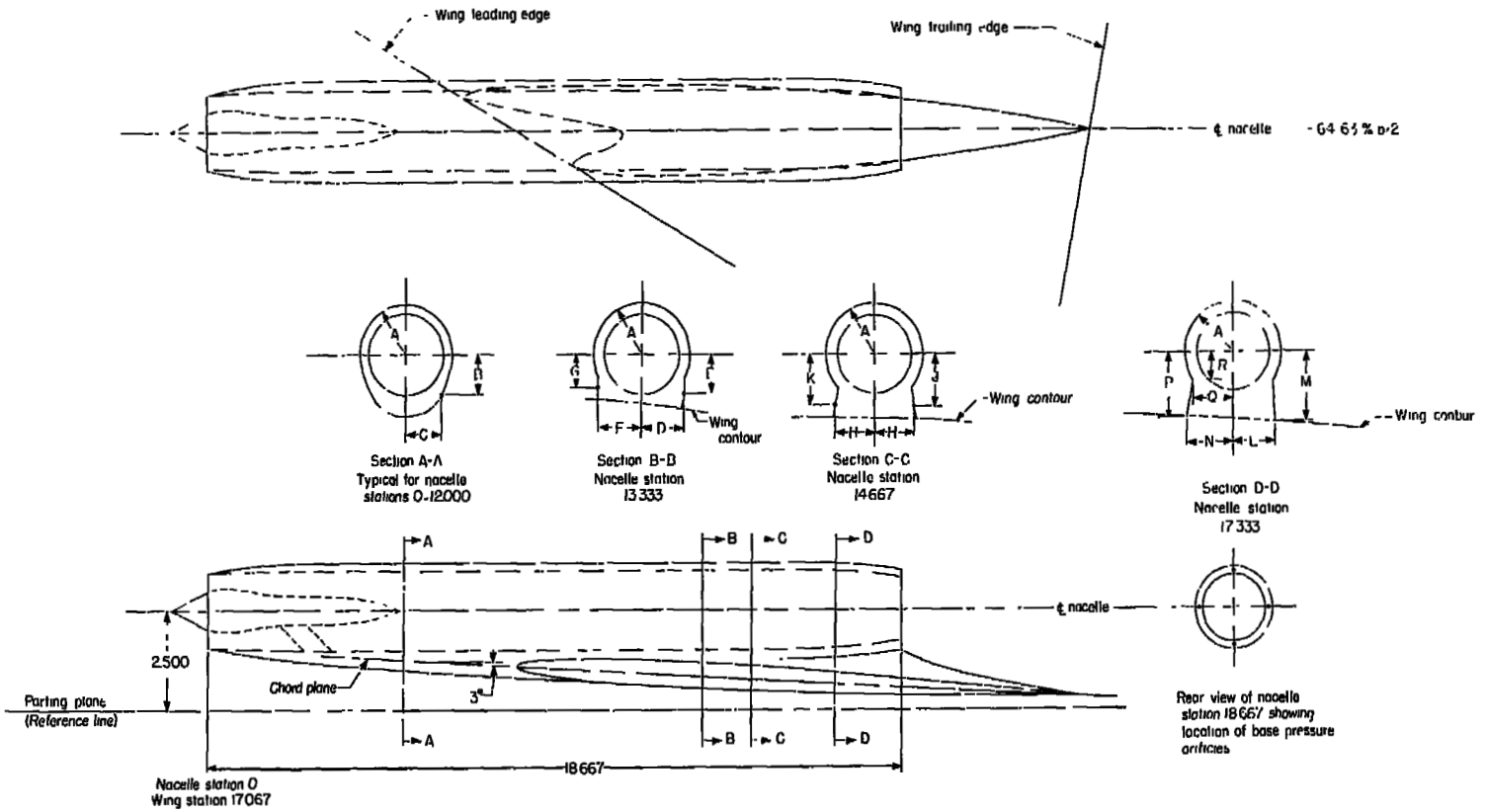

Figure 7.- Details of outboard split nacelle. See table VI for dimensions not given on the figure. (All dimensions are in inches.)

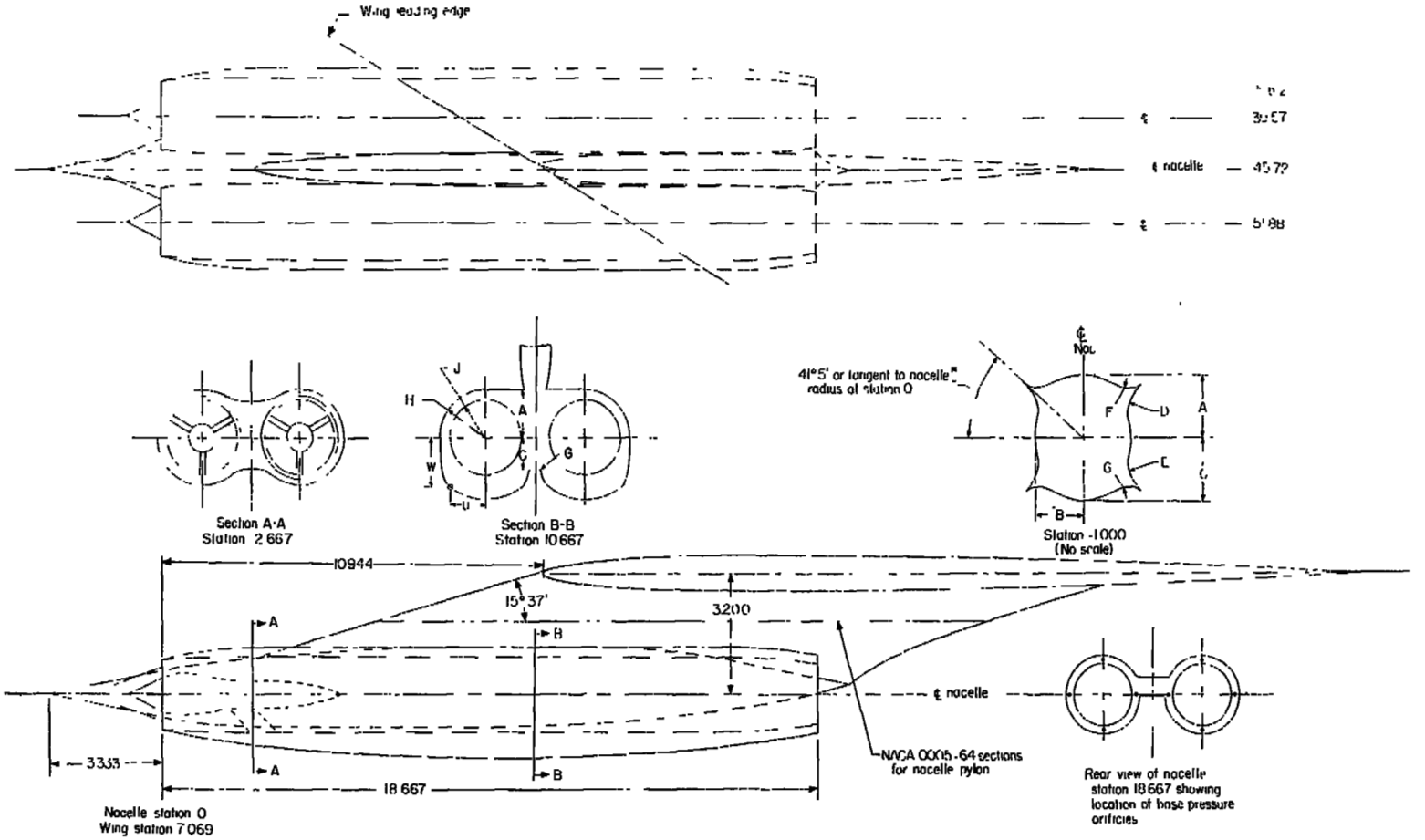

Figure 8.- Sketch of Siamese nacelle and strut. See table VII for dimensions not given on the figure. (All dimensions are in inches.)

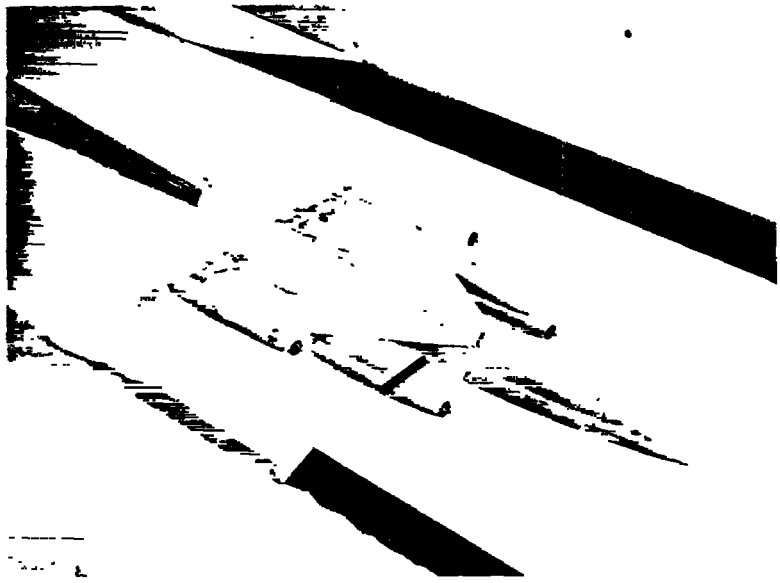

(a) Plane wing; split nacelles. L-81734

(b) Cambered wing; Siamese nacelles. L-81582

Figure 9.- Three-quarter front views of the four-engine delta-wing airplane model mounted in the Langley 16-foot transonic tunnel test section.

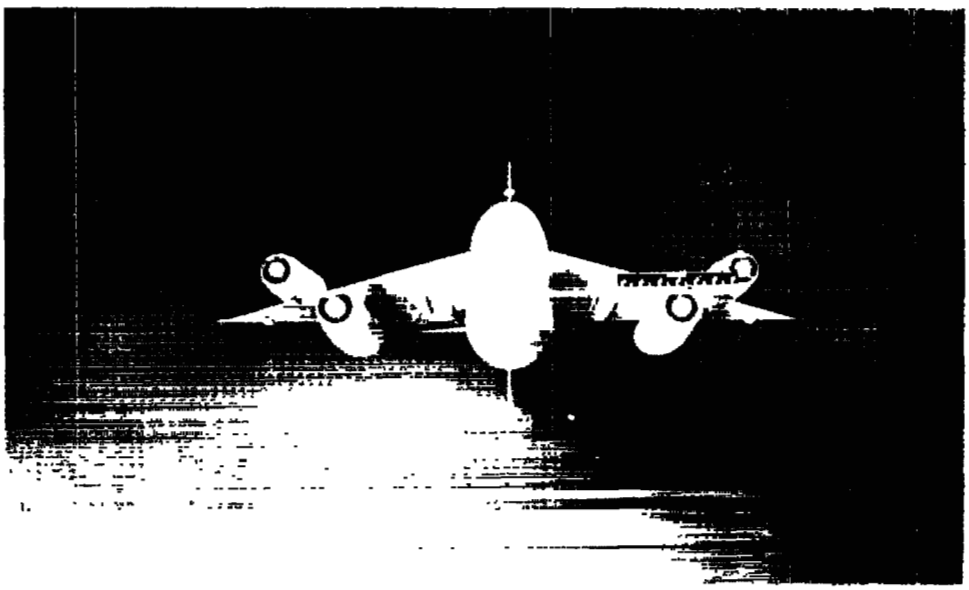

(a) Plane wing; split nacelles. L-81732

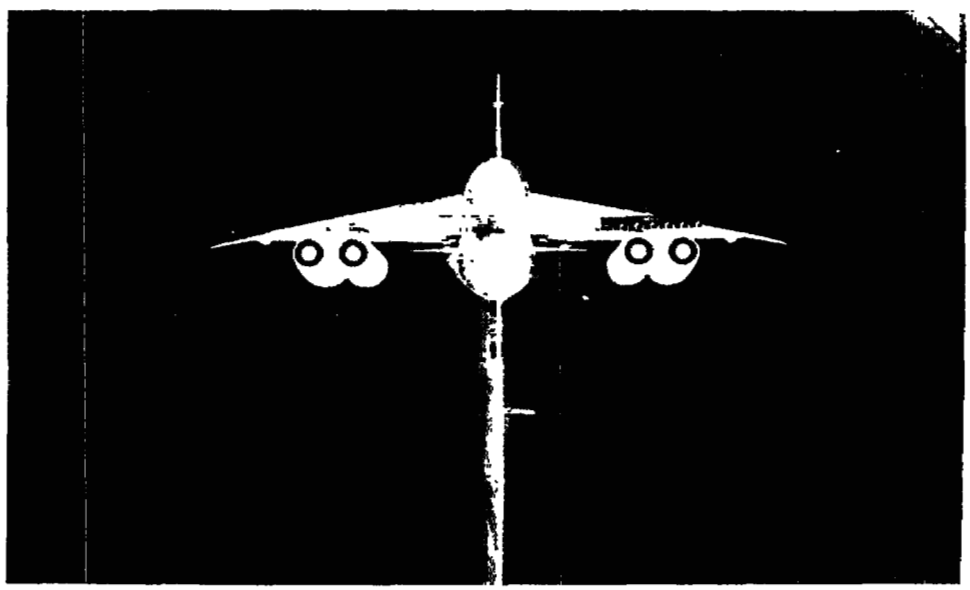

(b) Cambered wing; Siamese nacelles. L-81581

Figure 10.- Front views of the four-engine delta-wing airplane model mounted in the Langley 16-foot transonic tunnel test section.

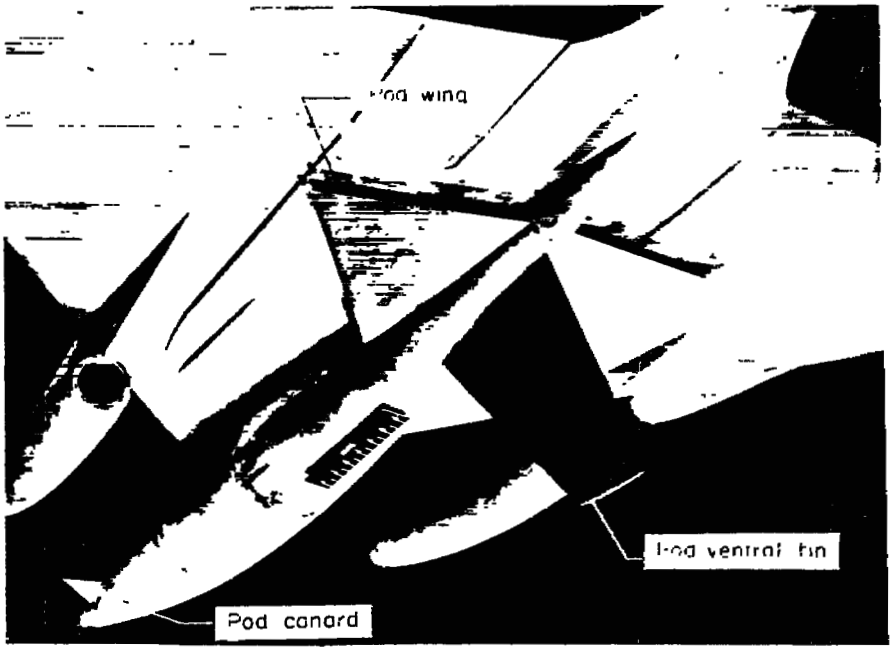

(a) Pod wing mounted on pod. L-81735.1

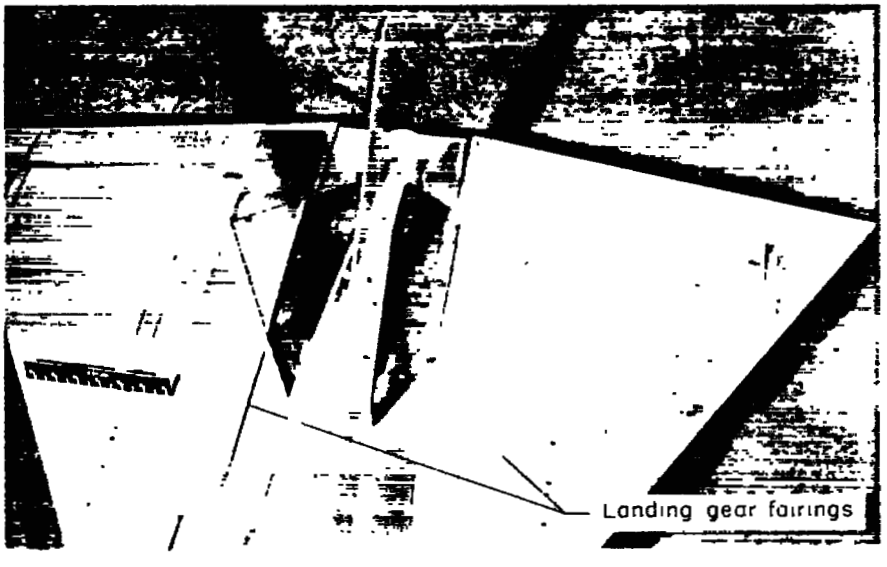

L-81731.1

(b) Pod wing mounted flush and faired into undersurface of main wing (nacelle removed).

Figure 11.- Bottom views of four-engine delta-wing airplane model.

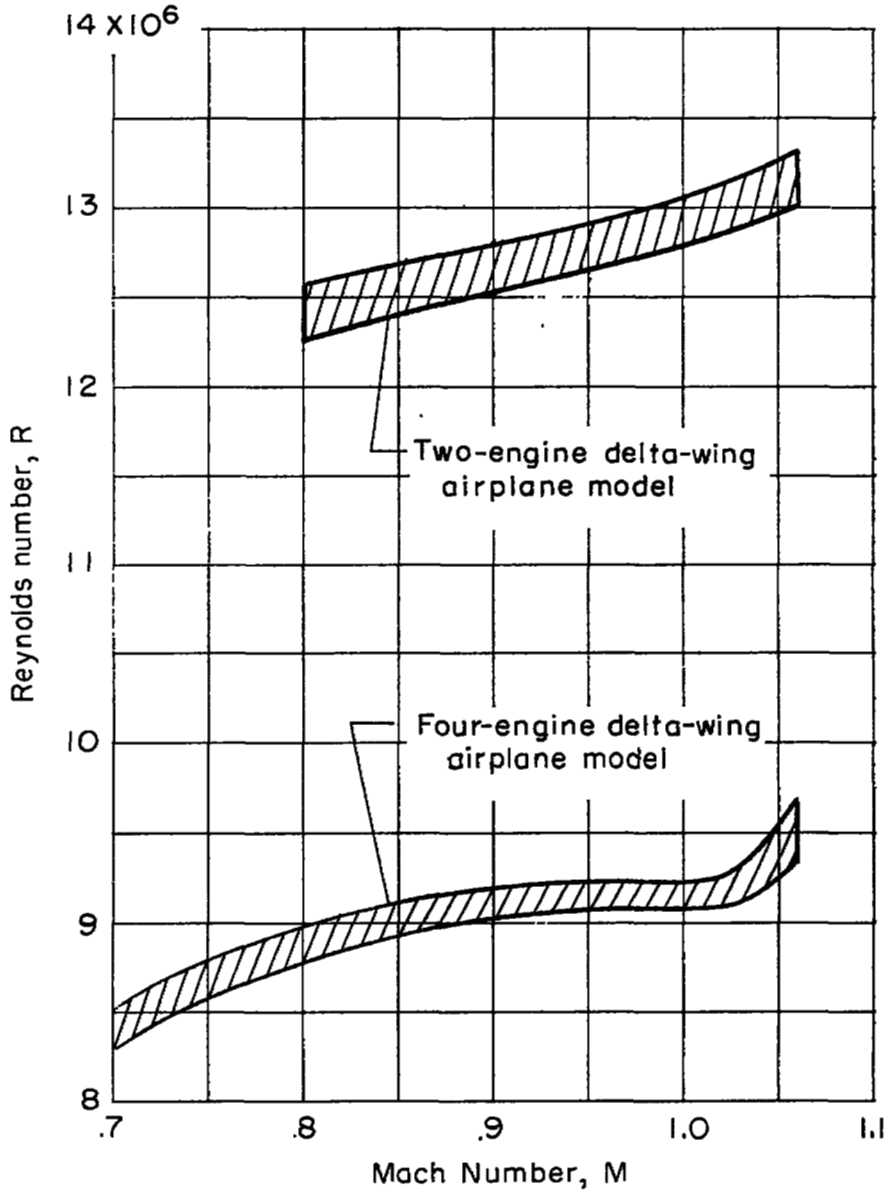

Figure 12.- Variation of Reynolds number with Mach number for the two-engine and four-engine delta-wing airplane models in the Langley 16-foot transonic tunnel.

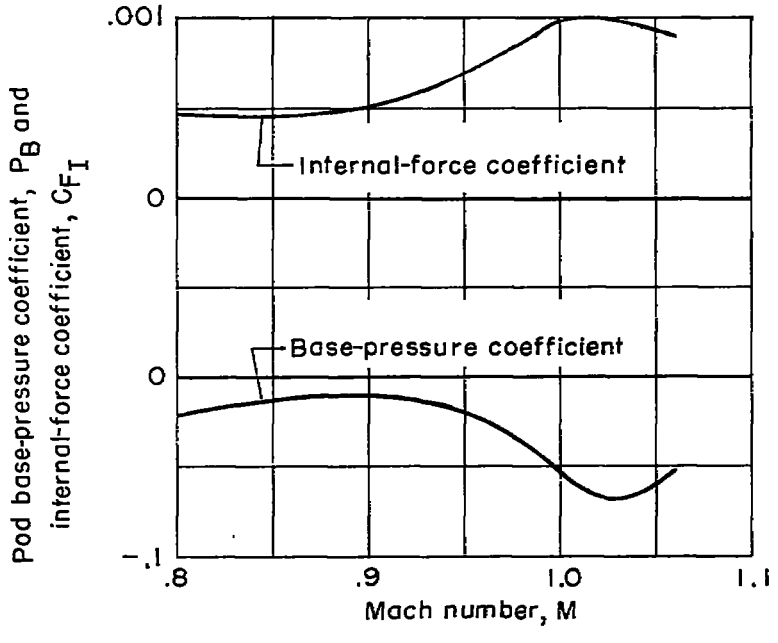

Figure 13.- Effect of Mach number on pod base-pressure coefficient and internal-force coefficient for two-engine delta-wing airplane model.

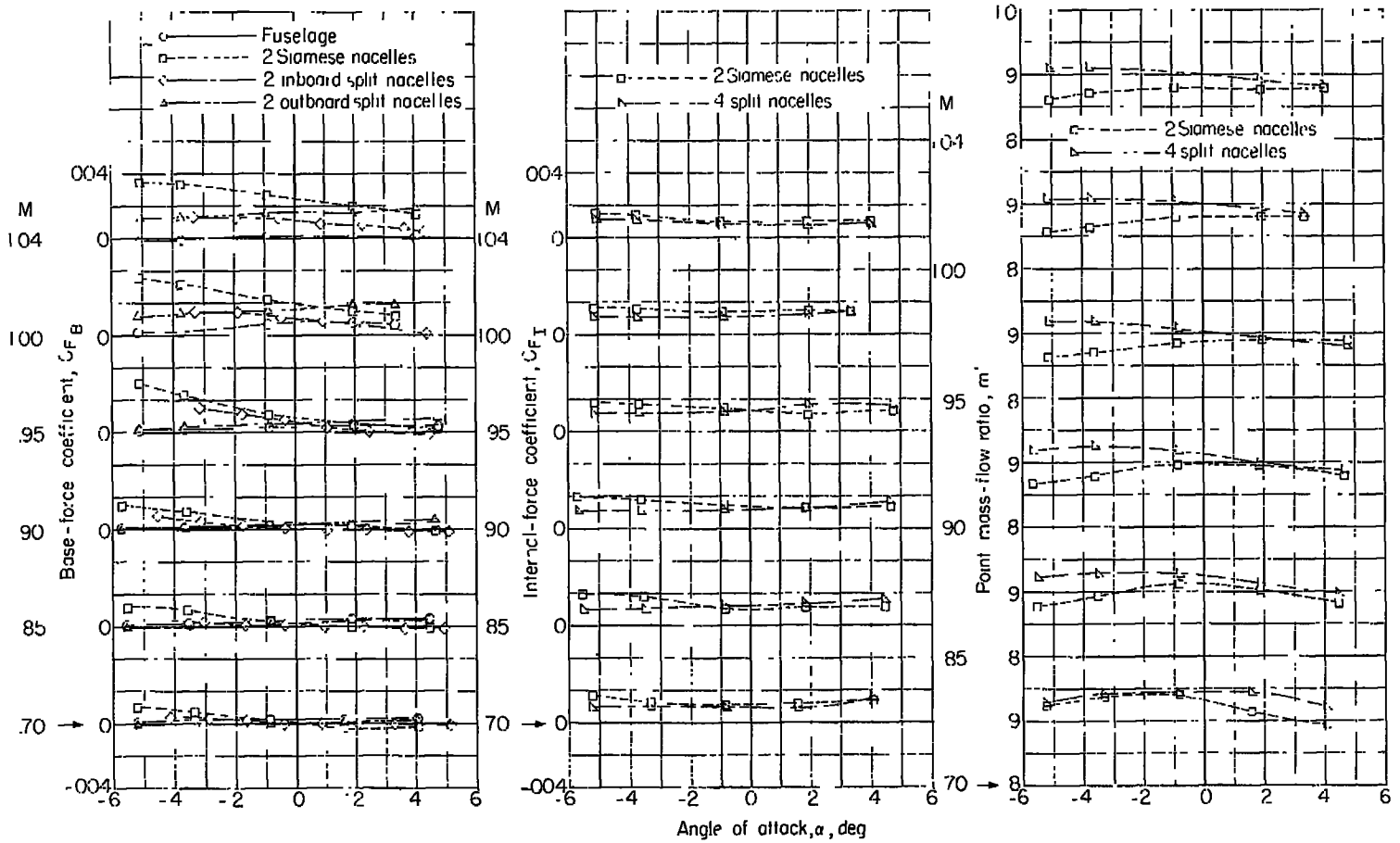

Figure 14.- Variation of base-force coefficient, internal-force coefficient, and point mass-flow ratio with angle of attack for a range of Mach numbers. Four-engine delta-wing airplane model with plane wing. $\delta = 0^{\circ}$.

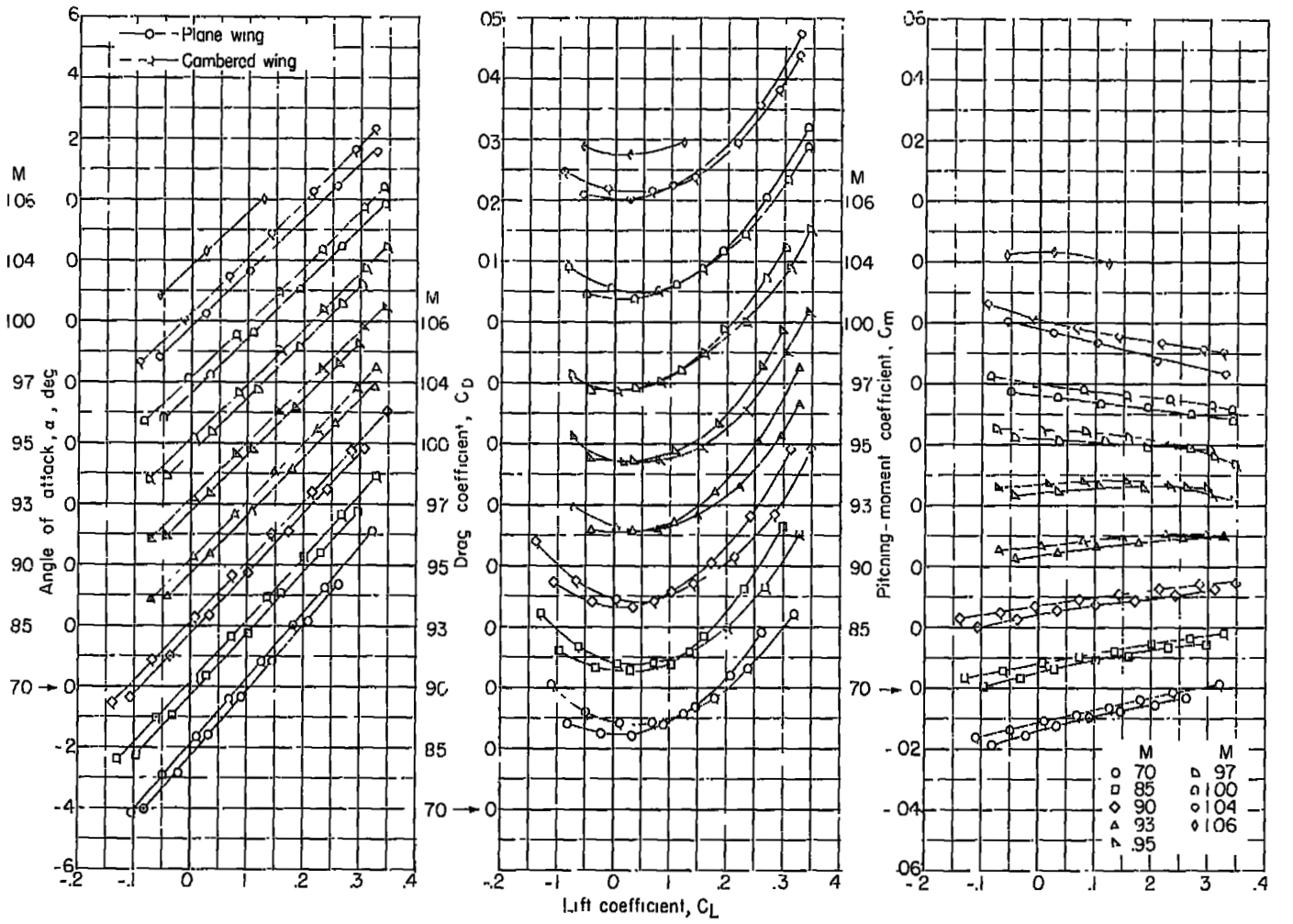

(a) $\delta = 0^\circ$.

Figure 15.- Aerodynamic characteristics of the four-engine delta-wing airplane models (plane and cambered wing) with split nacelles. Flagged symbols indicate cambered-wing model.

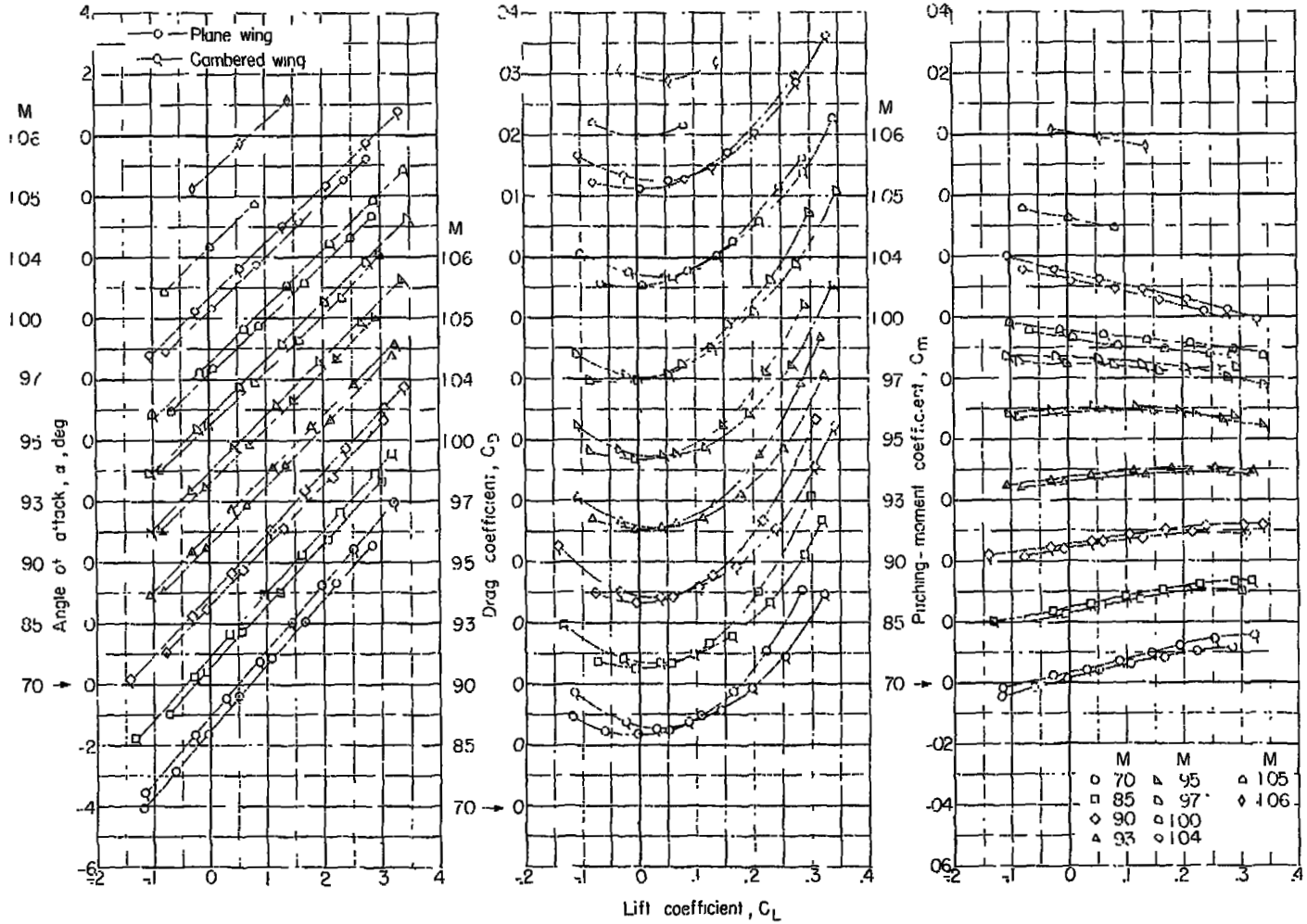

(b) $\delta = -2^{\circ}$.

Figure 15.- Continued.

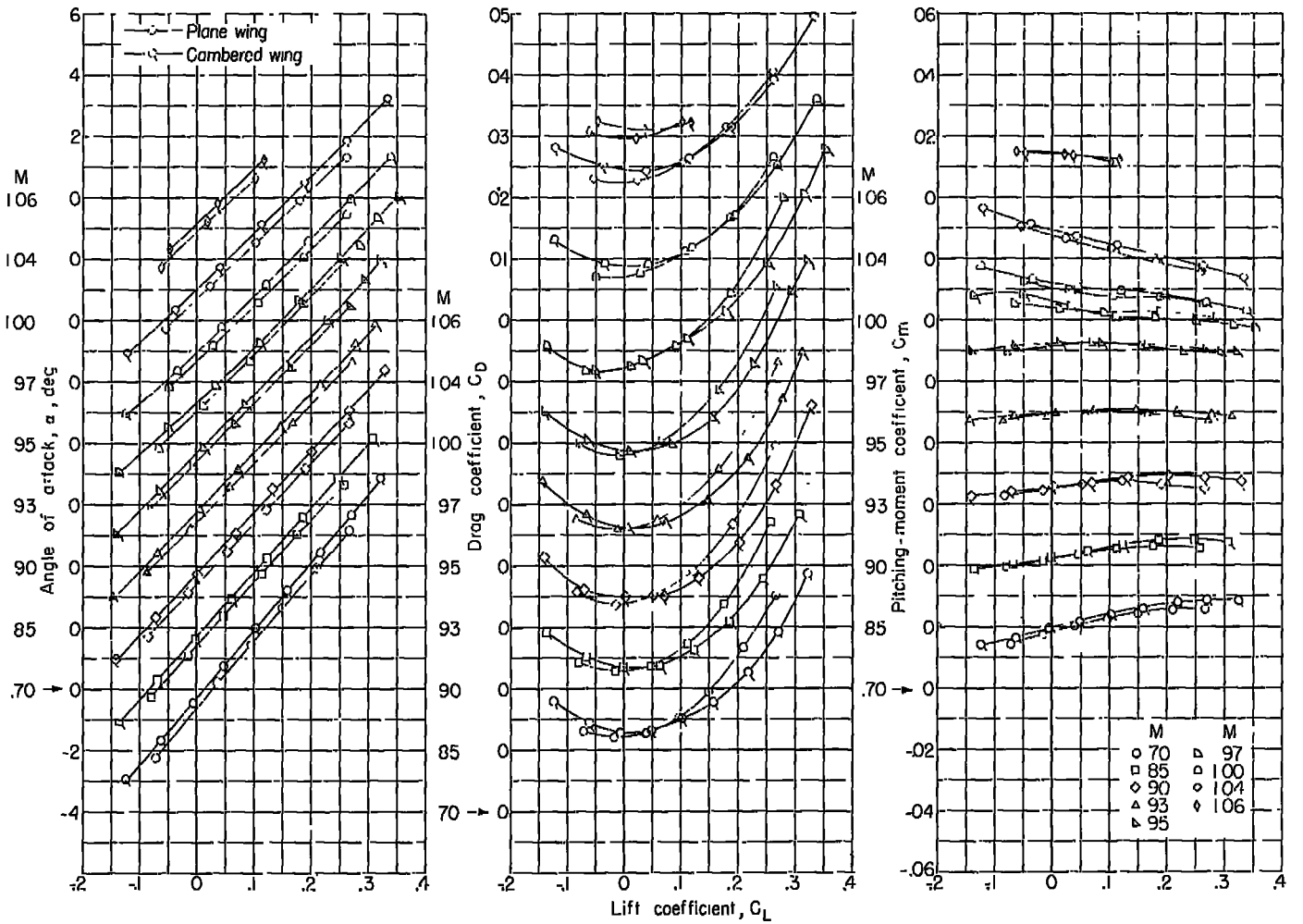

(c) $\delta = -4^\circ$.

Figure 15.- Concluded.

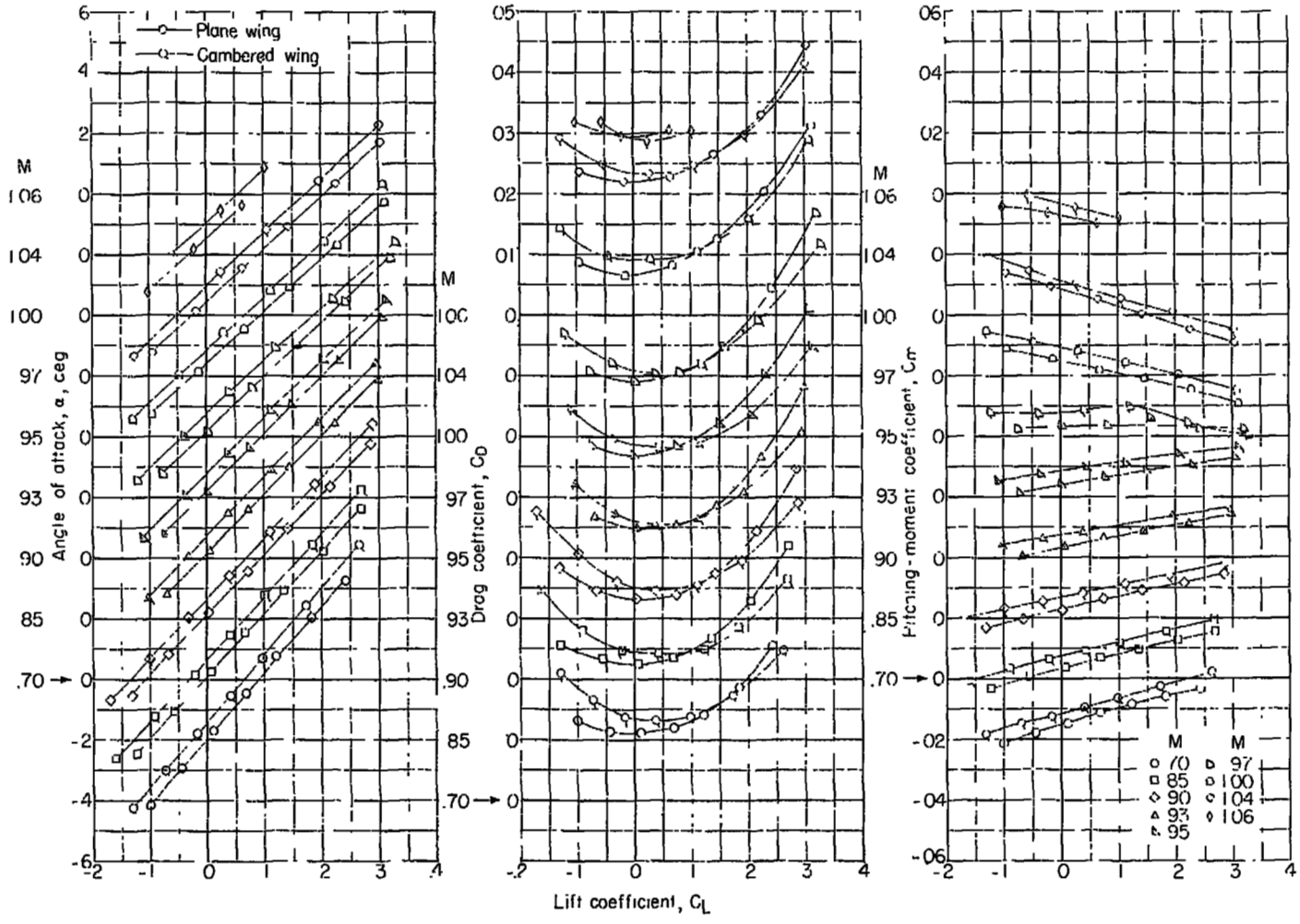

(a) Cambered wing and plane wing. $\delta = 0^{\circ}$.

Figure 16.- Aerodynamic characteristics of the four-engine delta-wing airplane models with Siamese nacelles.

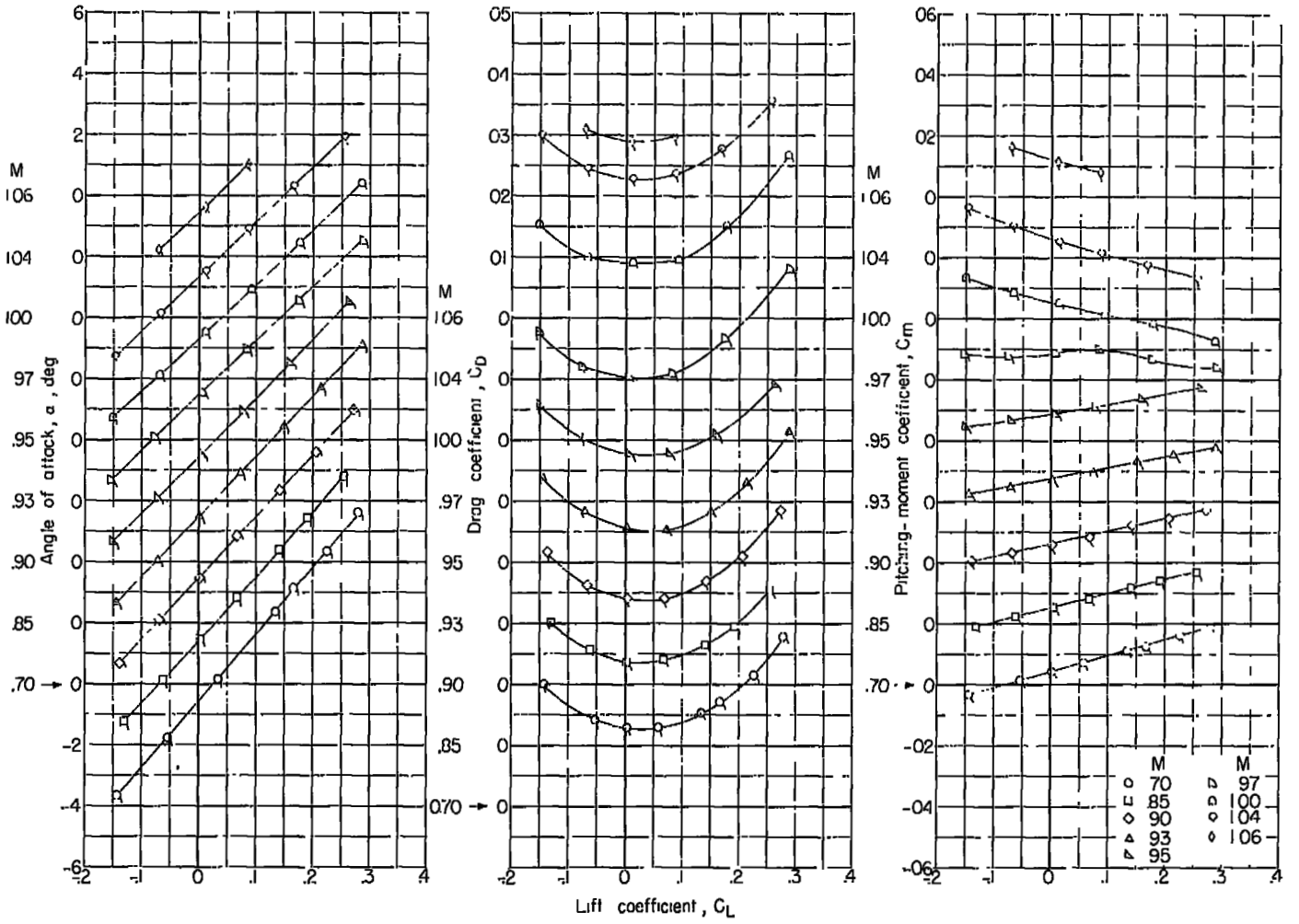

(b) Cambered wing, $\delta = -2^{\circ}$.

Figure 16.- Continued.

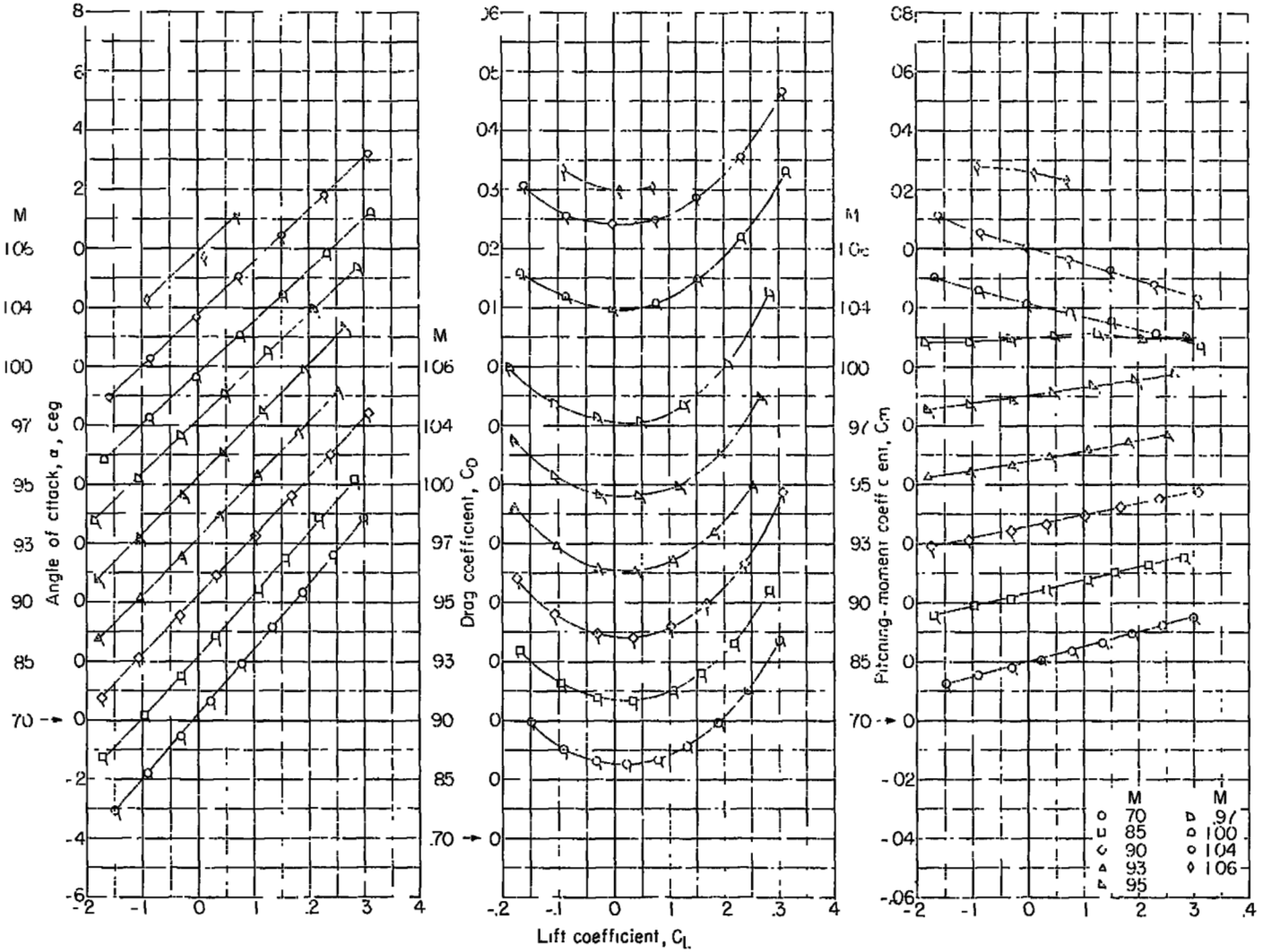

(c) Cambered wing, $\delta = -4^\circ$.

Figure 16.- Concluded.

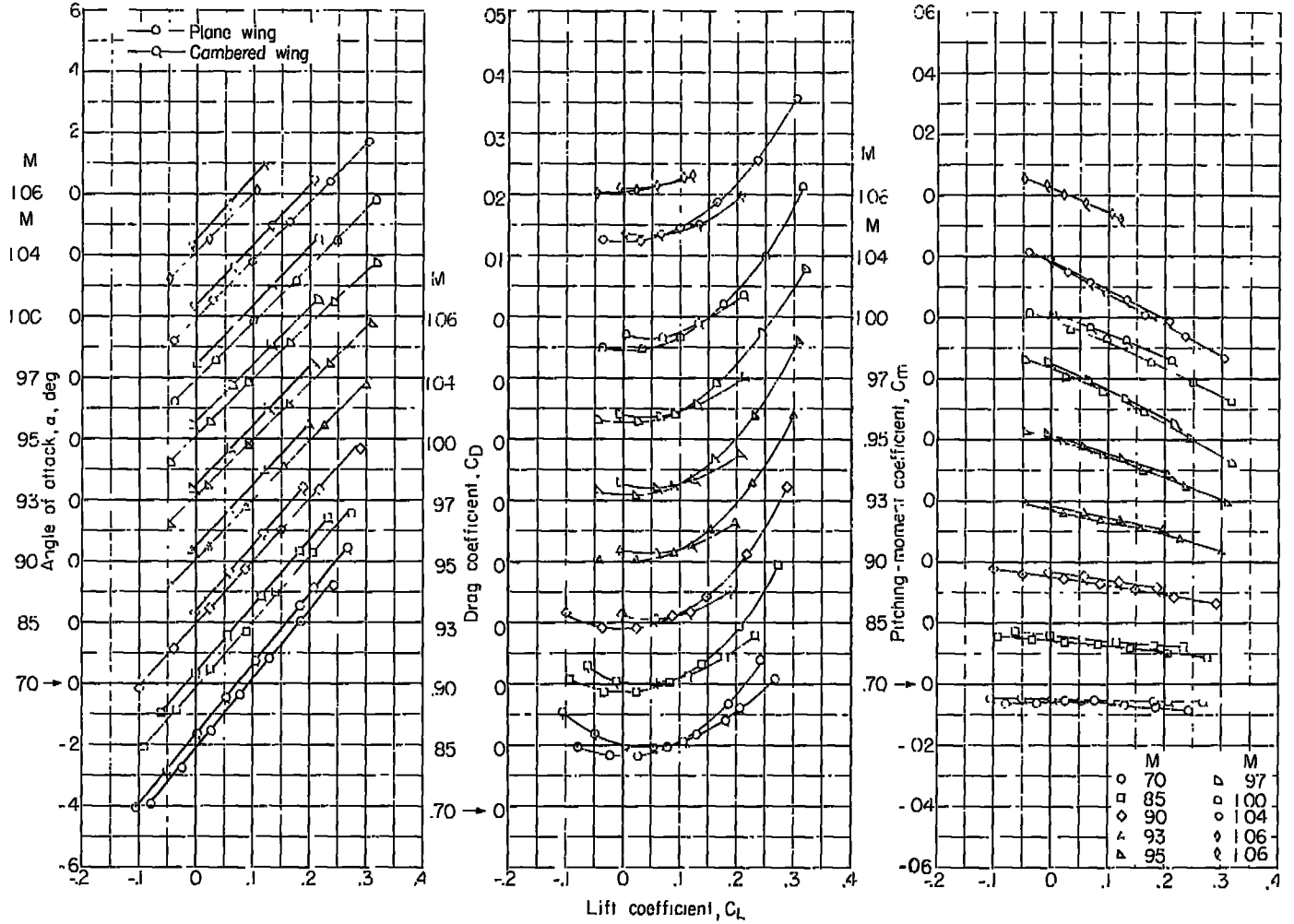

Figure 17.- Aerodynamic characteristics of the four-engine delta-wing airplane models (cambered wing and plane wing) without nacelles. $\delta = 0^{\circ}$. Flagged symbols indicate cambered-wing model.

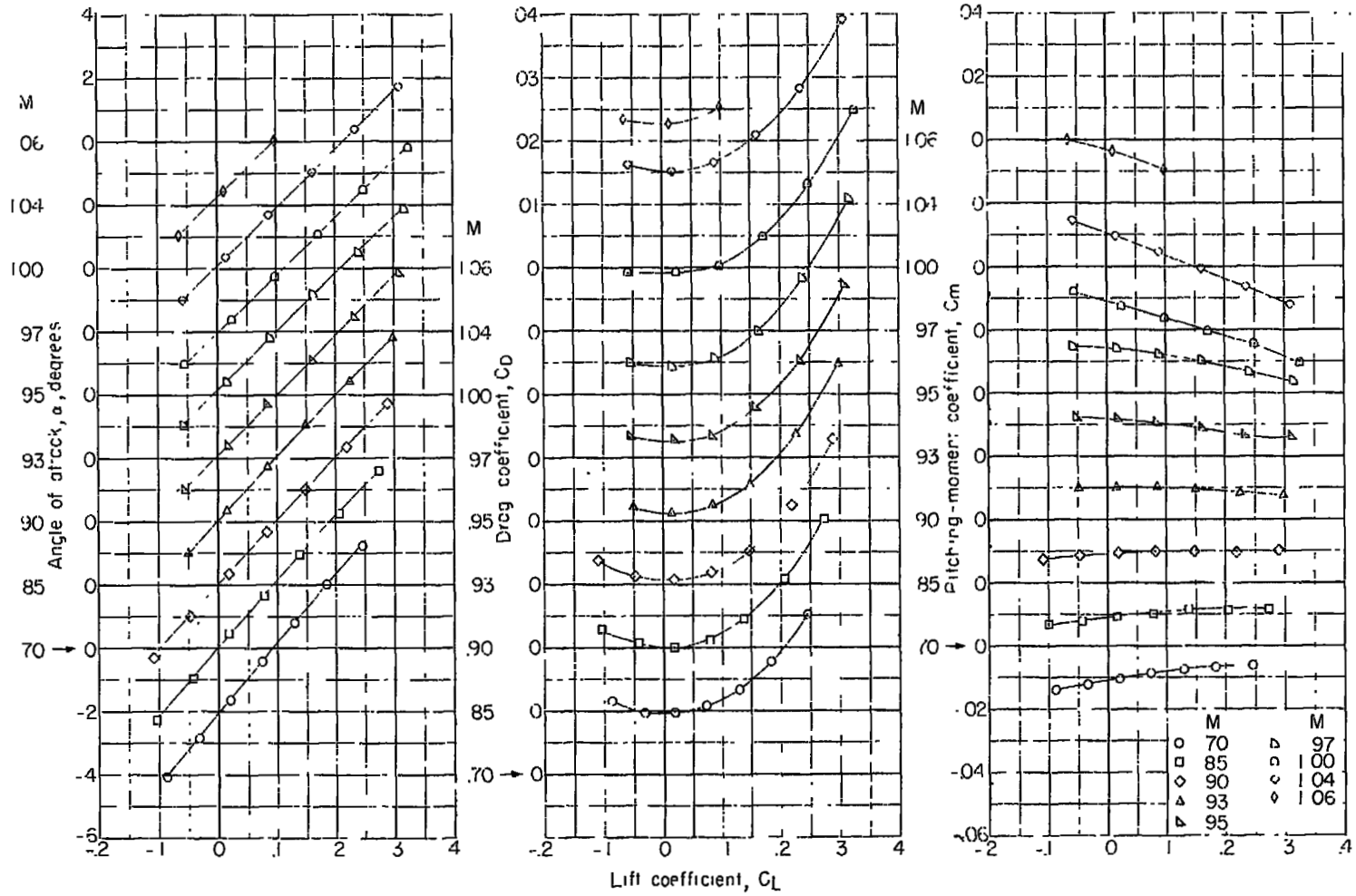

Figure 18.- Aerodynamic characteristics of the four-engine delta-wing airplane model with plane wing and outboard nacelles off. $\delta = 0^{\circ}$.

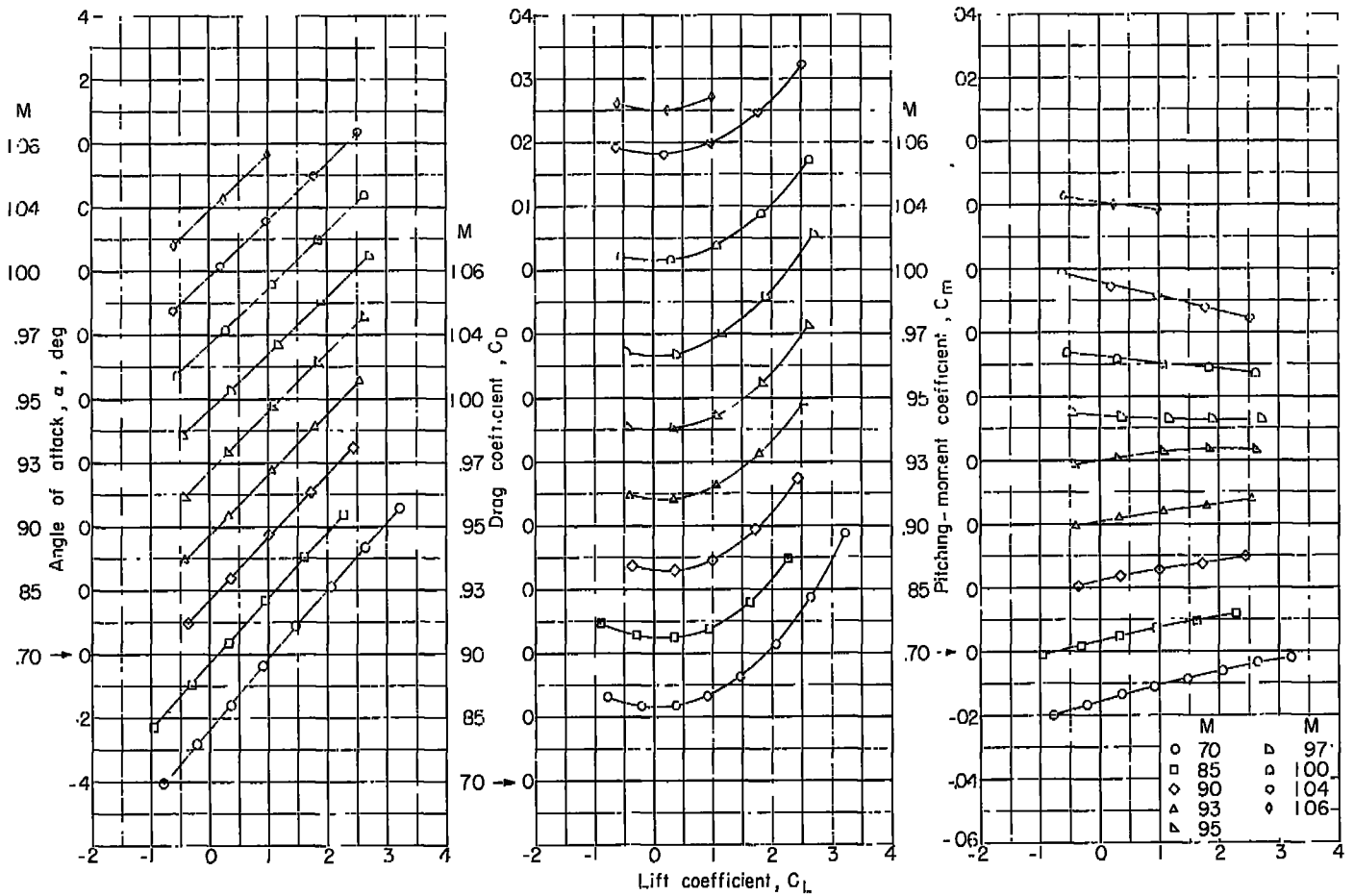

(a) Pod wing off.

Figure 19.- Aerodynamic characteristics of the four-engine delta-wing airplane model with plane-wing split nacelles for several pod modifications. $\delta = 0^{o}$.

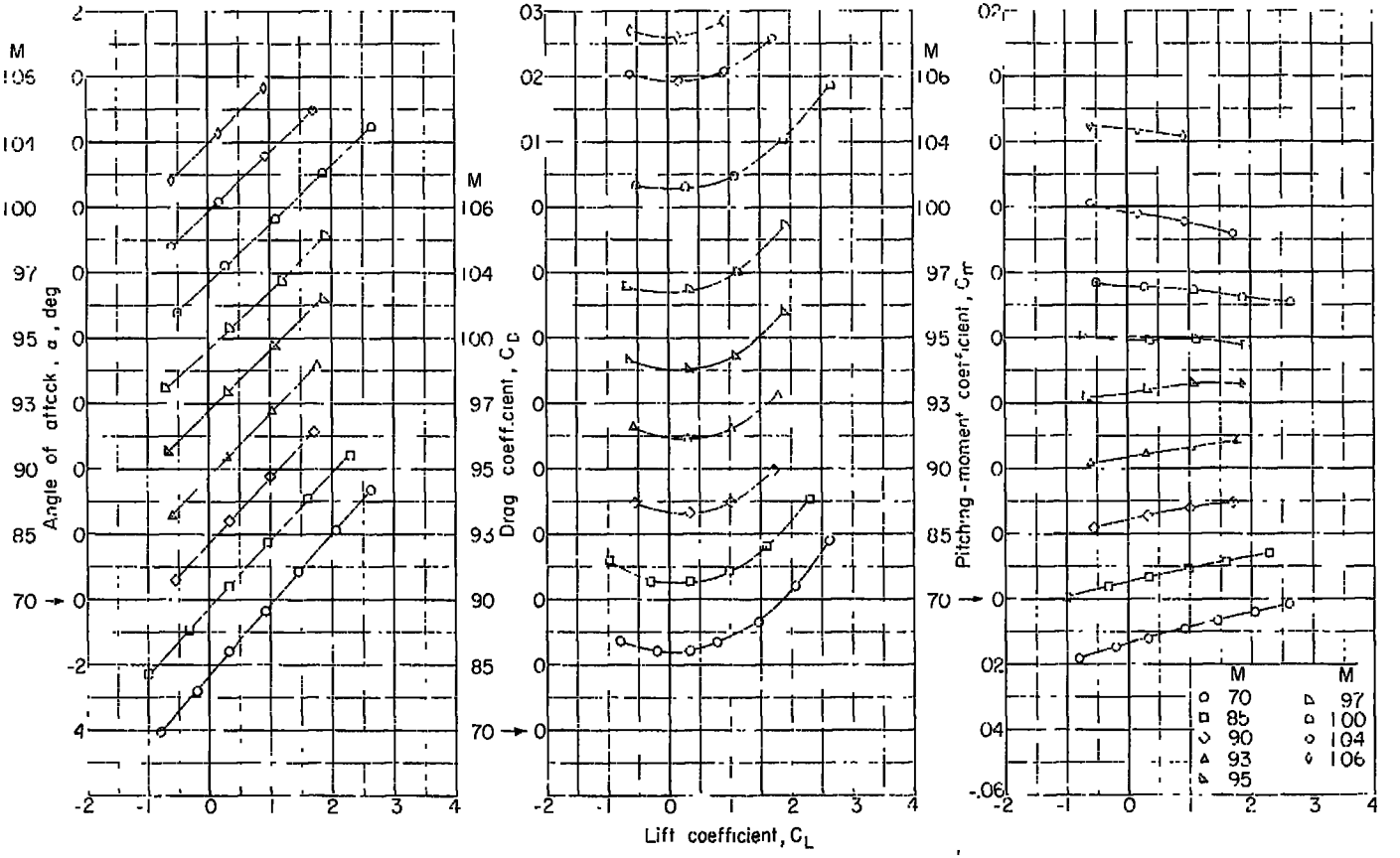

(b) Pod wing faired into undersurface of main wing.

Figure 19.- Continued.

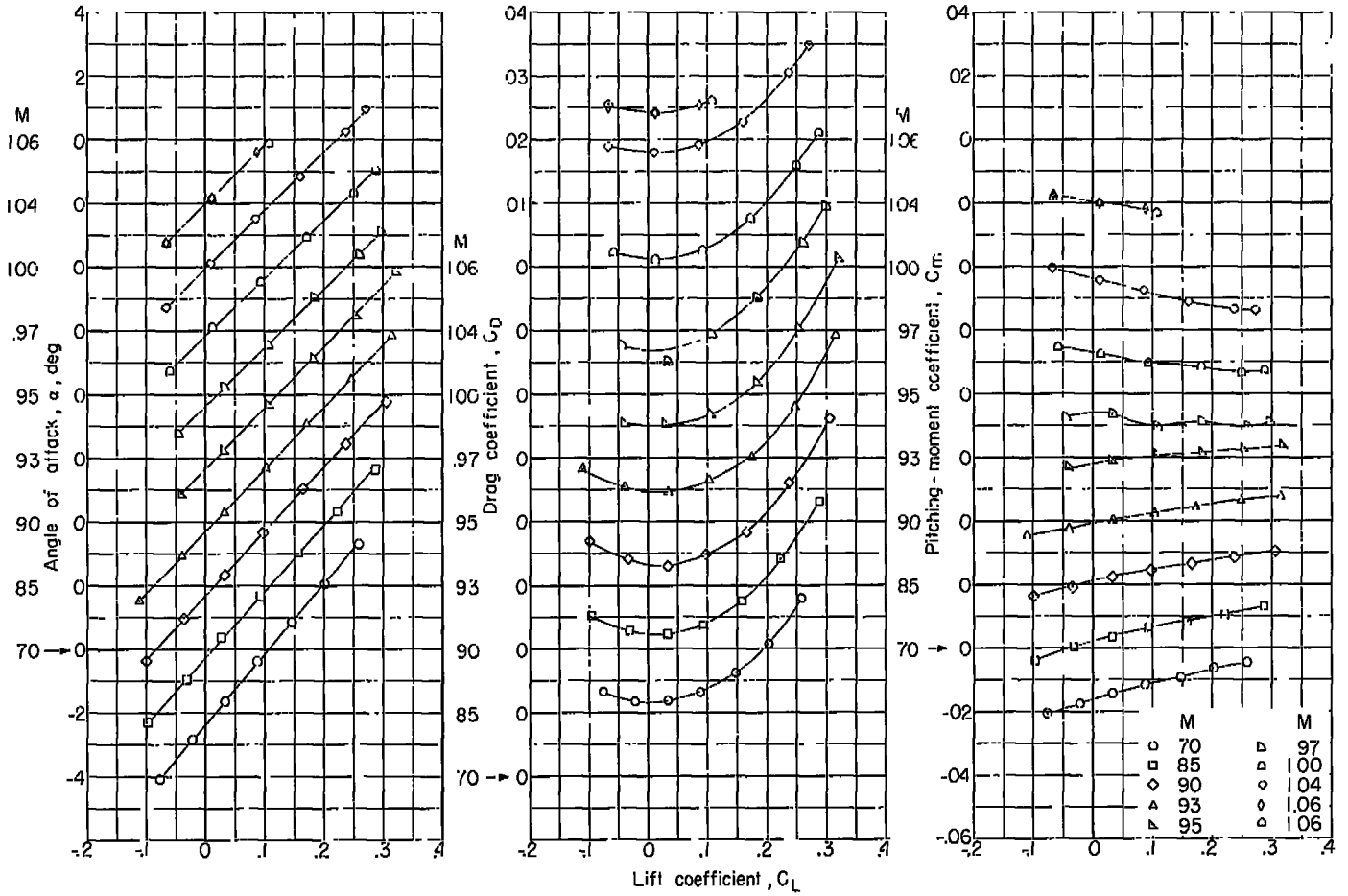

(c) Pod wing and ventral fin off.

Figure 19.- Continued.

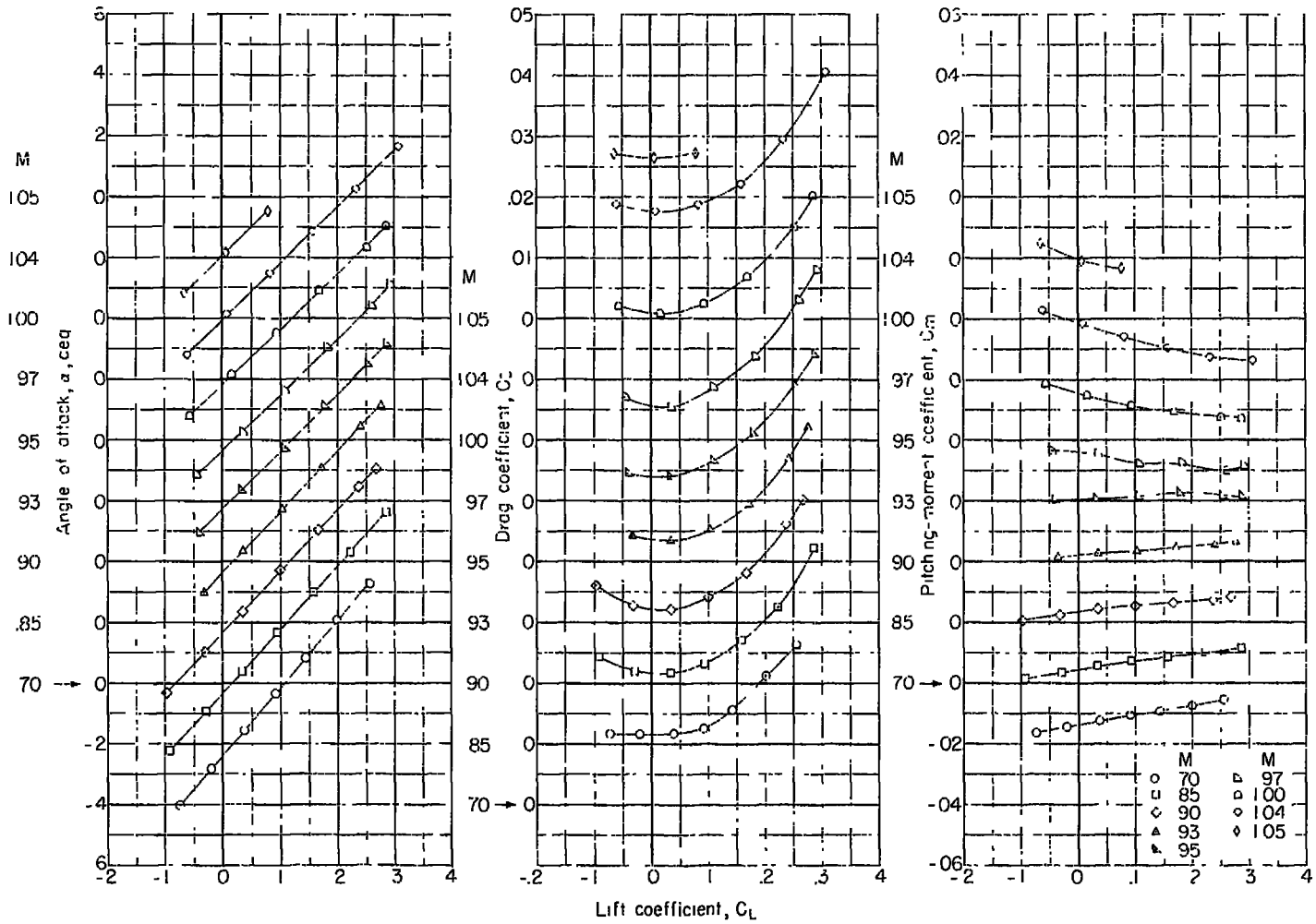

(d) Pod wing, ventral fin, and canard off.

Figure 19.- Concluded.

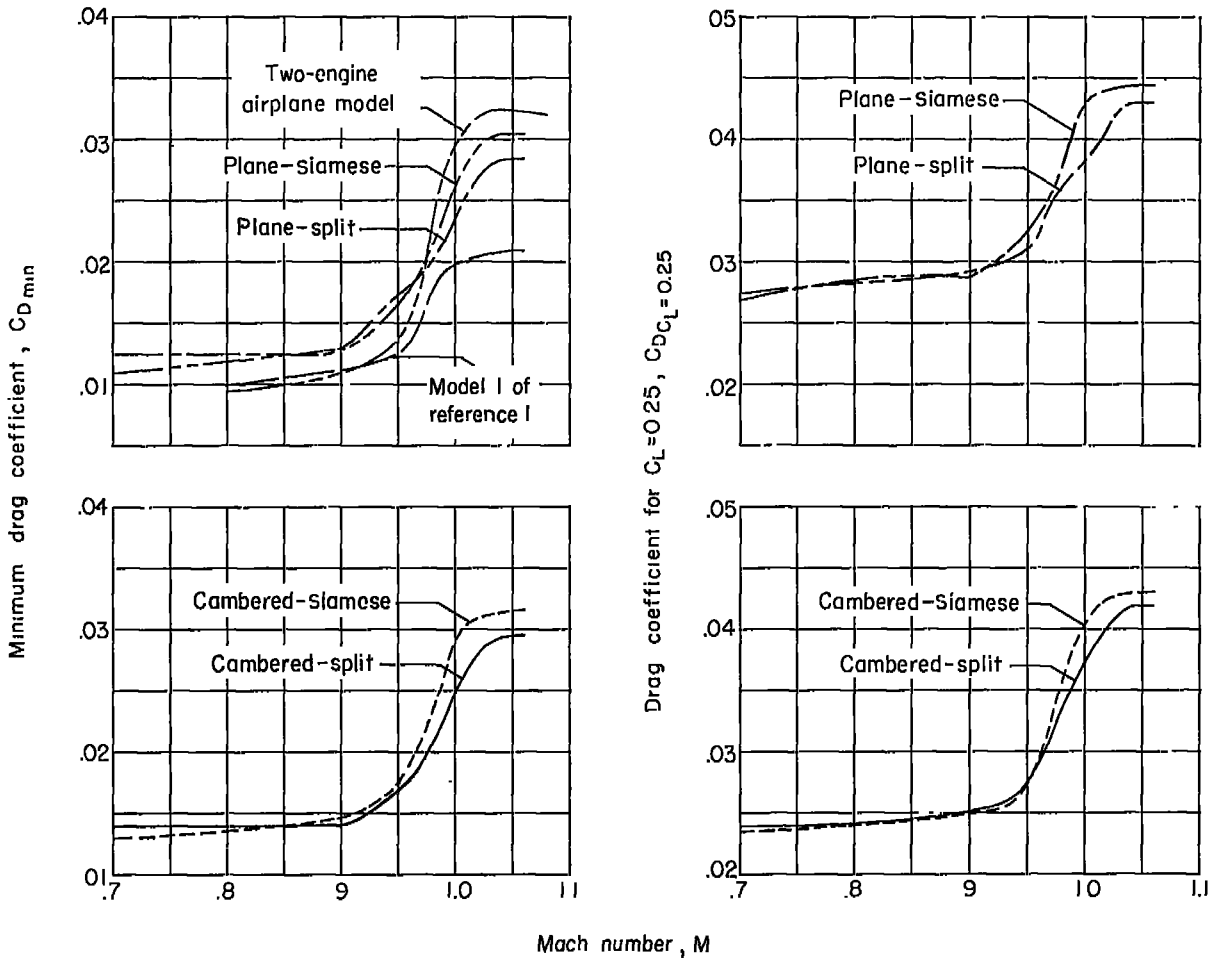

(a) C_D against M.

Figure 20.- Variation of drag coefficient with Mach number and cross-sectional area diagrams for the four-engine and two-engine delta-wing airplane models and model 1 (ref. 1). $\delta = 0^o$.

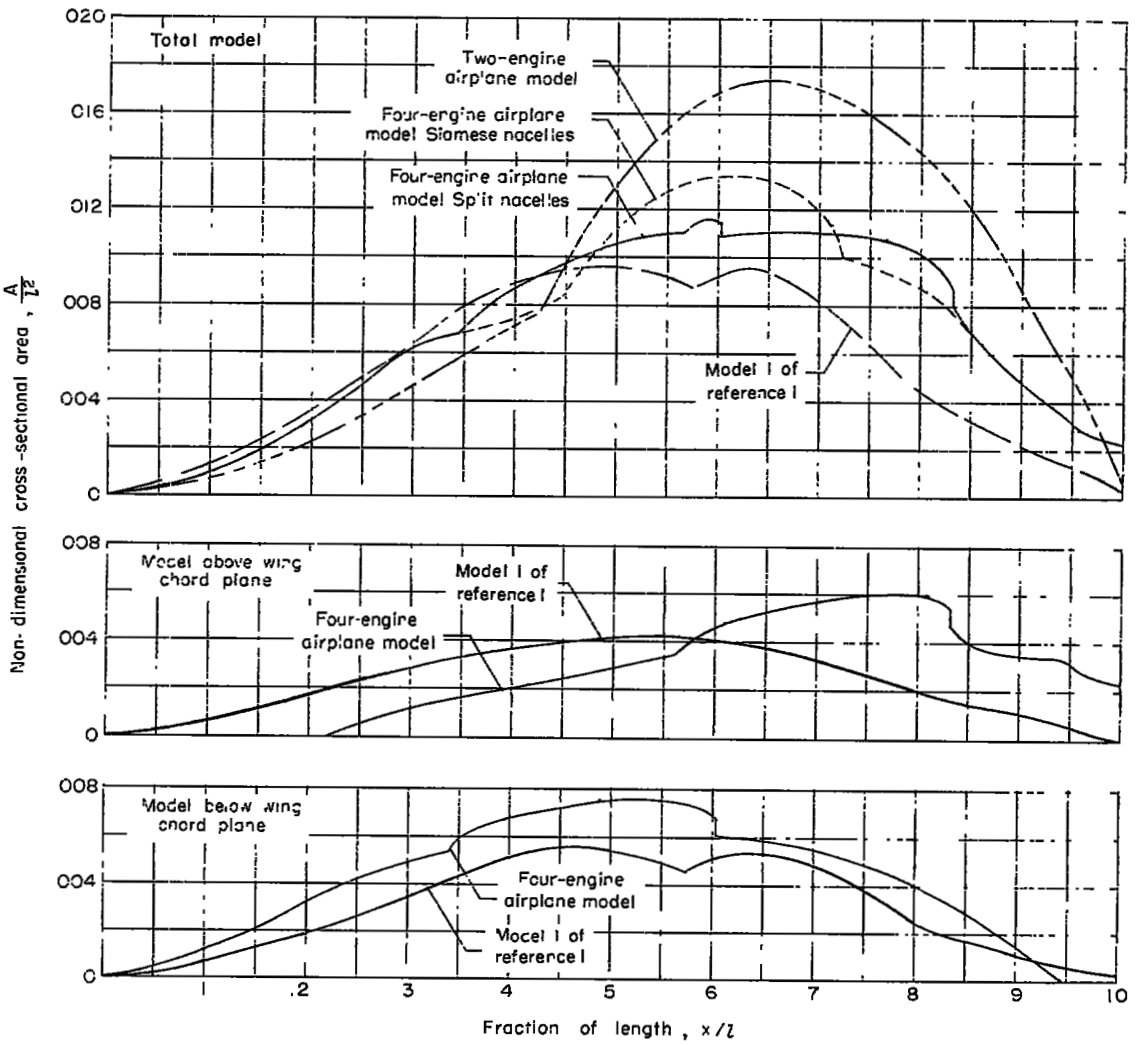

(b) Area diagrams.

Figure 20.- Concluded.

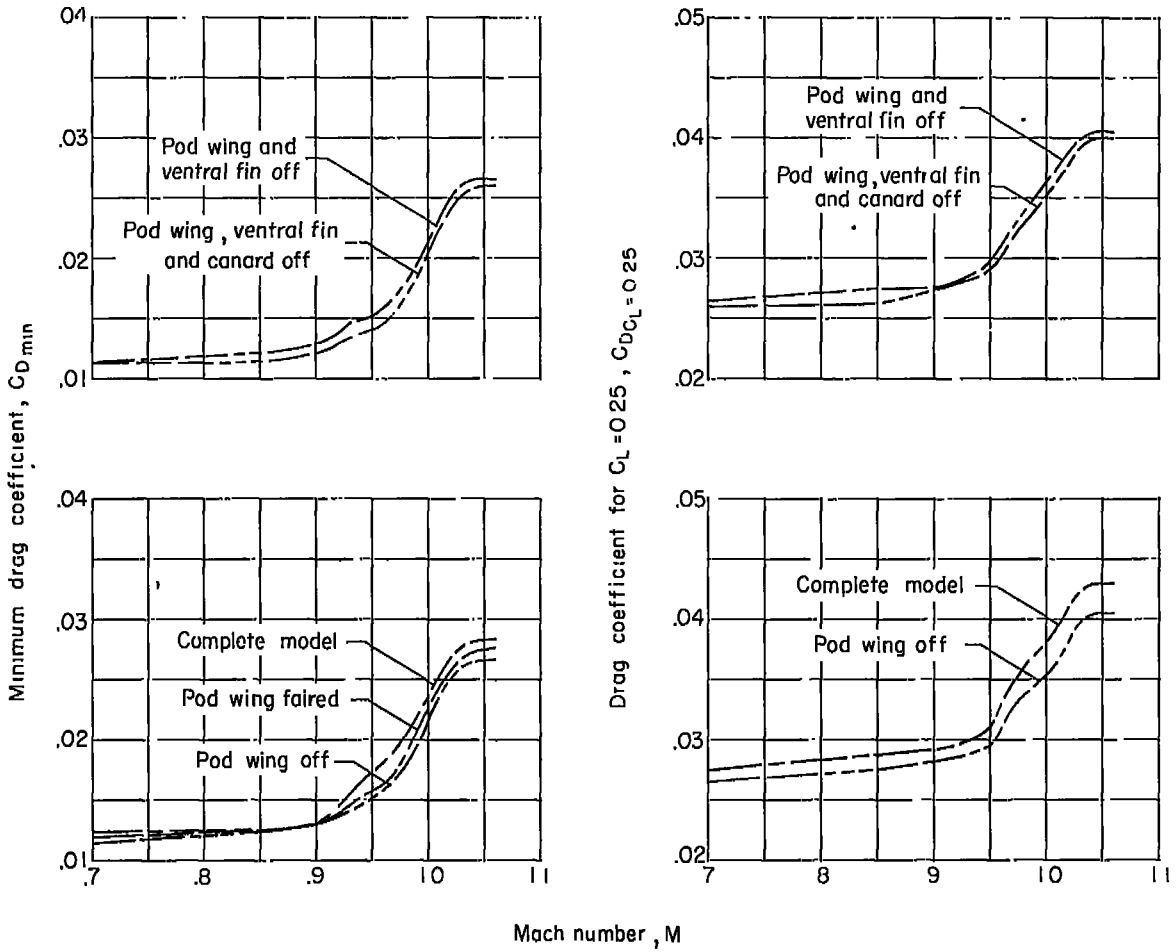

(a) C_D against M.

Figure 21.- Variation of drag coefficient with Mach number and cross-sectional area diagrams of the four-engine delta-wing airplane model with plane-wing split nacelles for various pod modifications. $\delta = 0^o$.

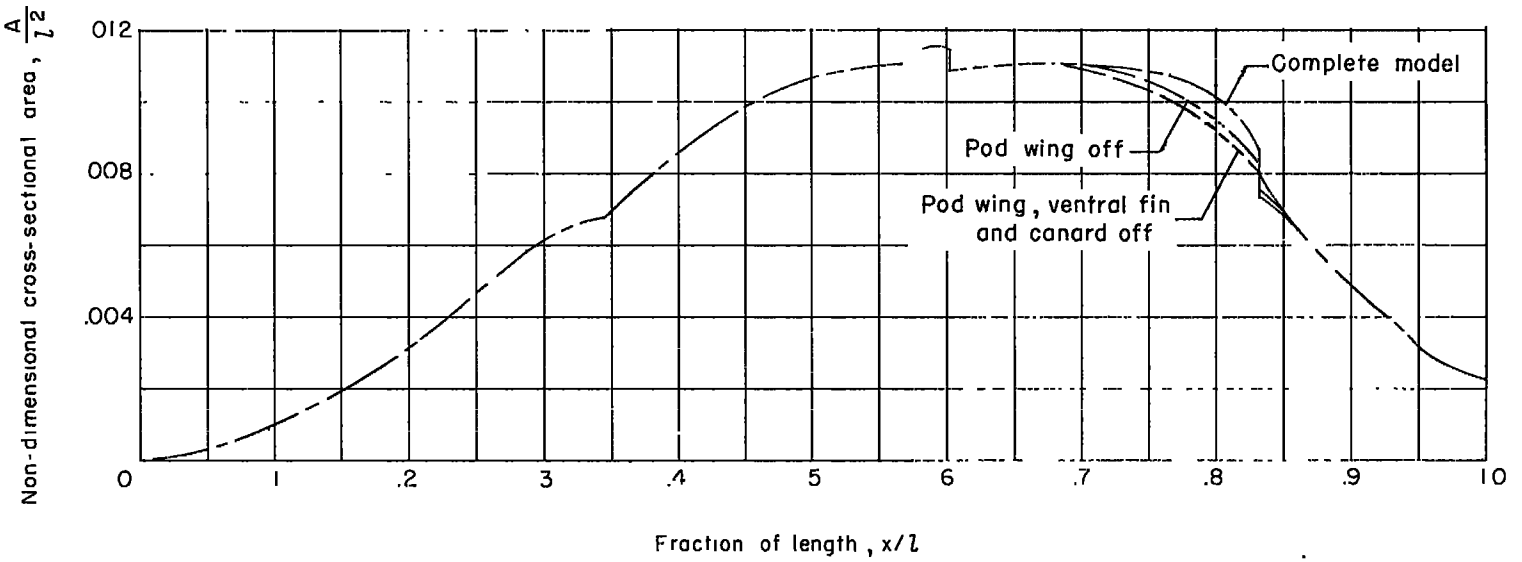

(b) Area diagrams.

Figure 21.- Concluded.

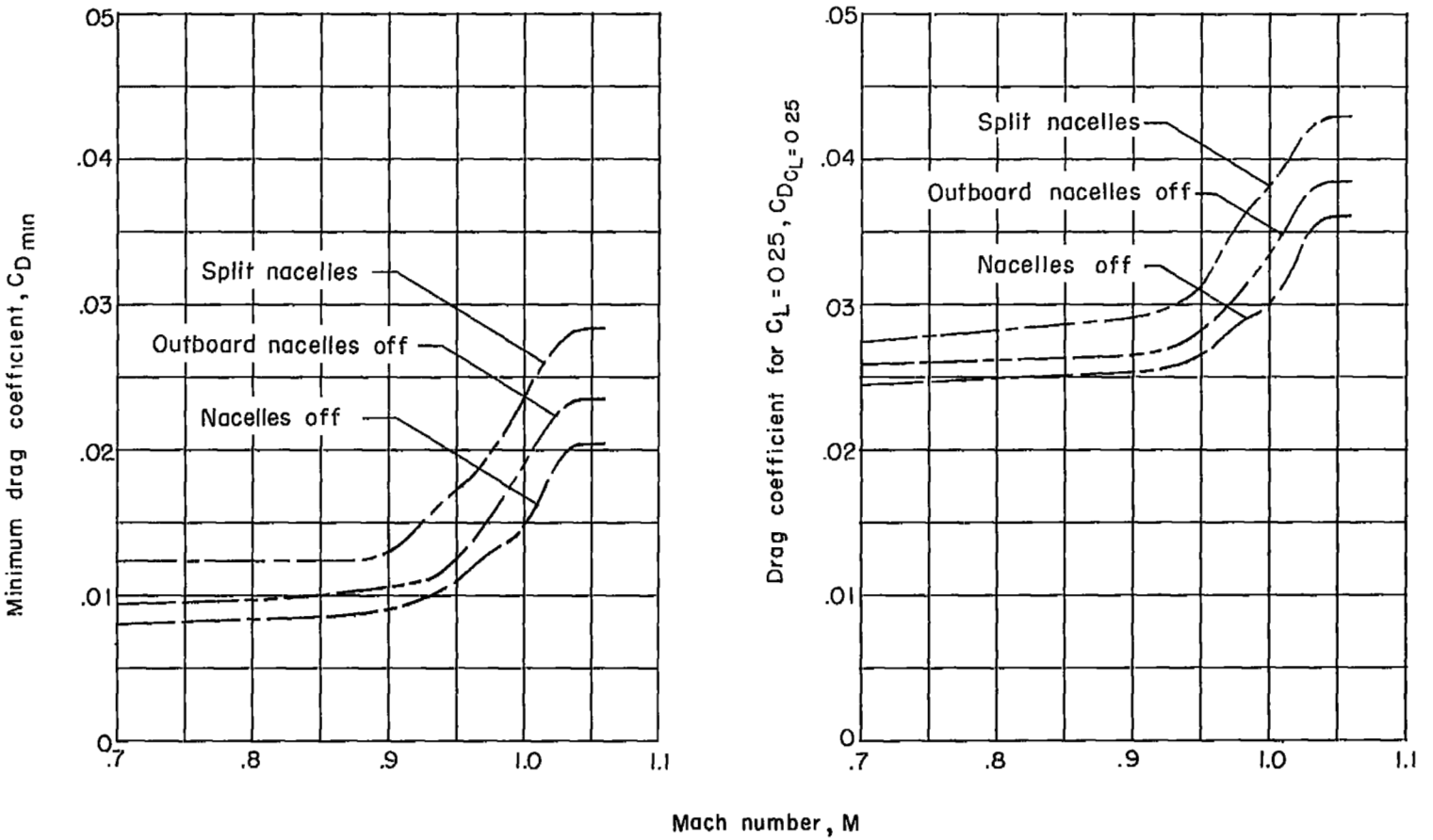

(a) C_D against M.

Figure 22.- Variation of drag coefficient with Mach number and cross-sectional area diagrams of the four-engine delta-wing airplane model with plane wing for several nacelle configurations. $\delta = 0^o$.

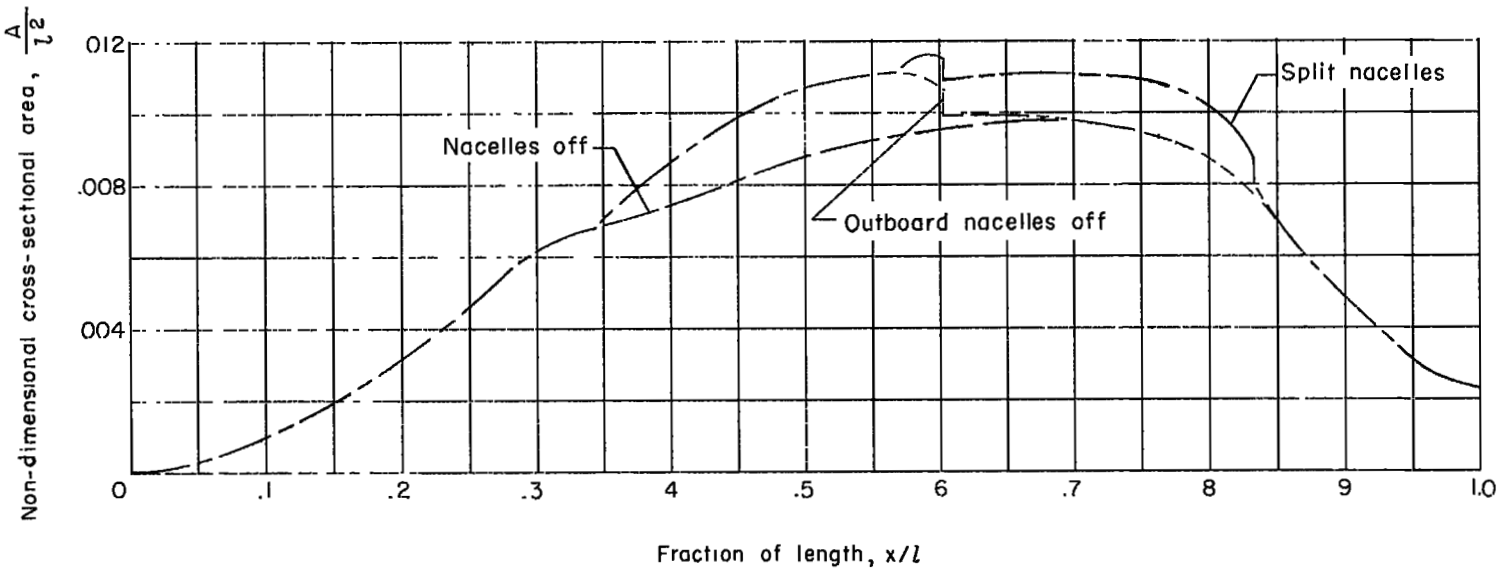

(b) Area diagrams.

Figure 22.- Concluded.

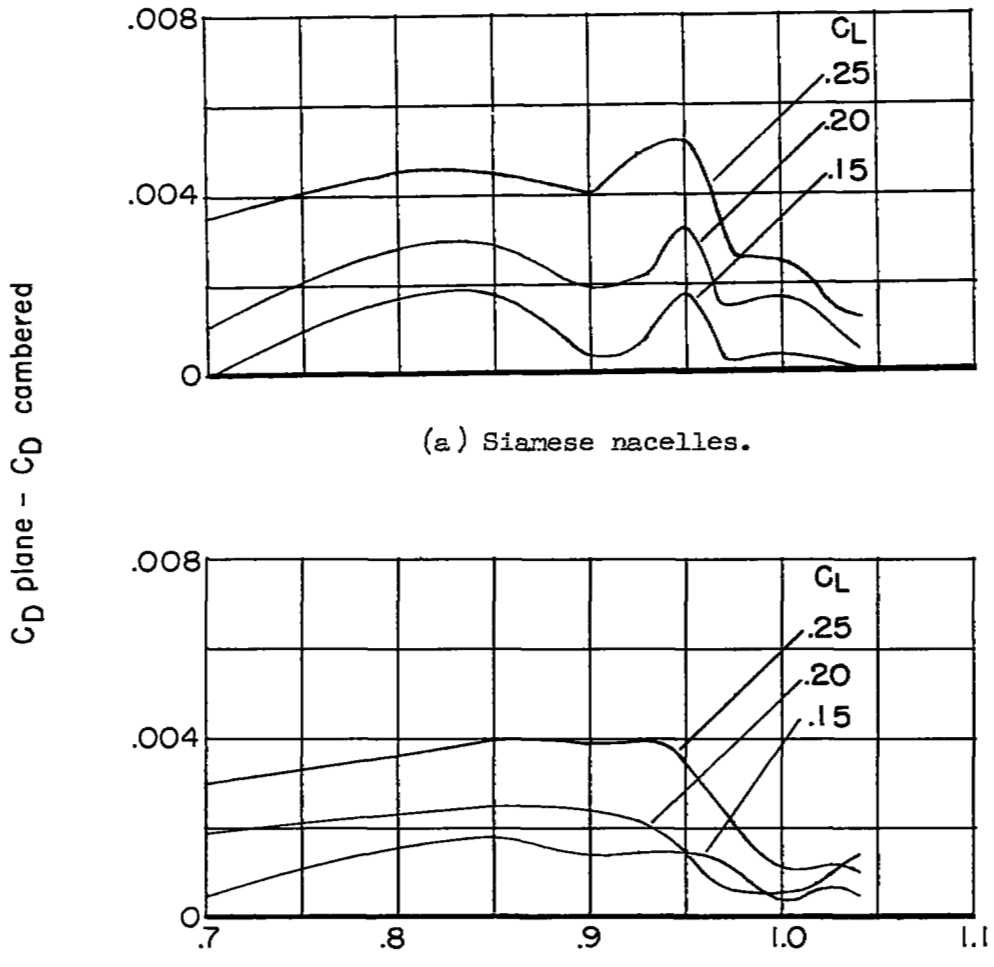

(a) Siamese nacelles.

(b) Split nacelles.

Figure 23.- Effect of Mach number on the reduction in drag coefficient due to camber at lift coefficients of 0.15, 0.20, and 0.25 for the four-engine delta-wing airplane models. $\delta = 0^{\circ}$.

[redacted]

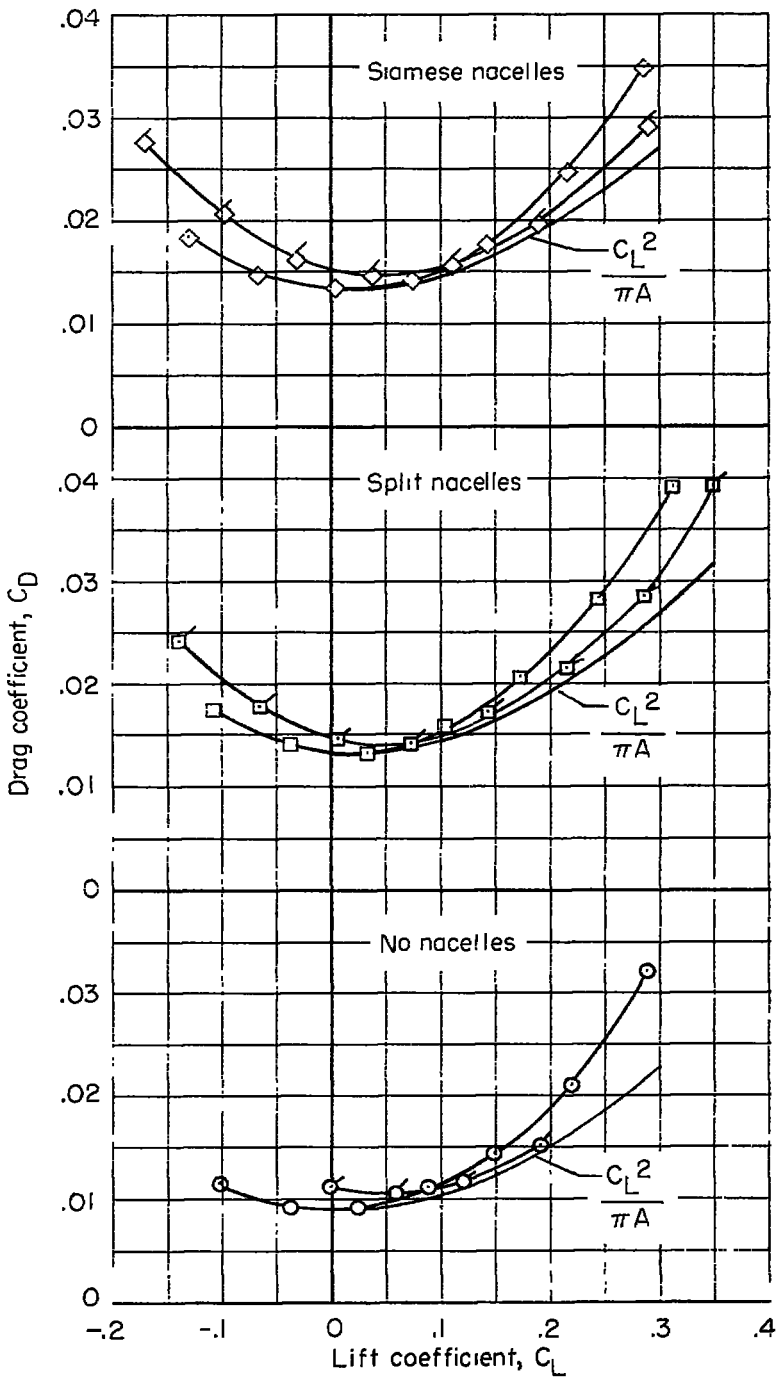

Figure 24.- Effect of camber on drag due to lift at a Mach number of 0.90 for the four-engine delta-wing airplane models. $\delta = 0^\circ$. (Flagged symbols are for cambered wing.)

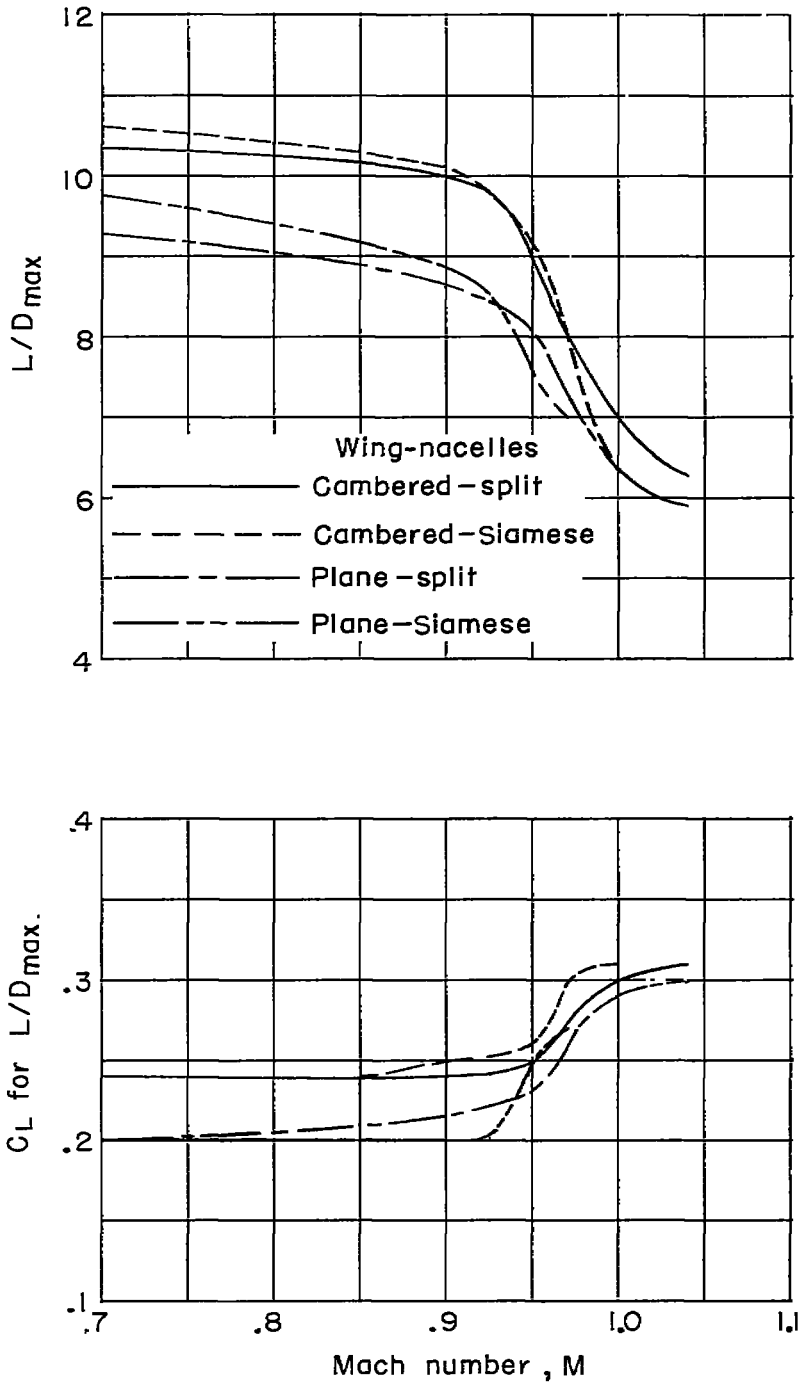

Figure 25.- Variation of maximum lift-drag ratio and lift coefficient for maximum lift-drag ratio with Mach number for the four-engine delta-wing airplane models. $\delta = 0^{\circ}$.

[redacted]

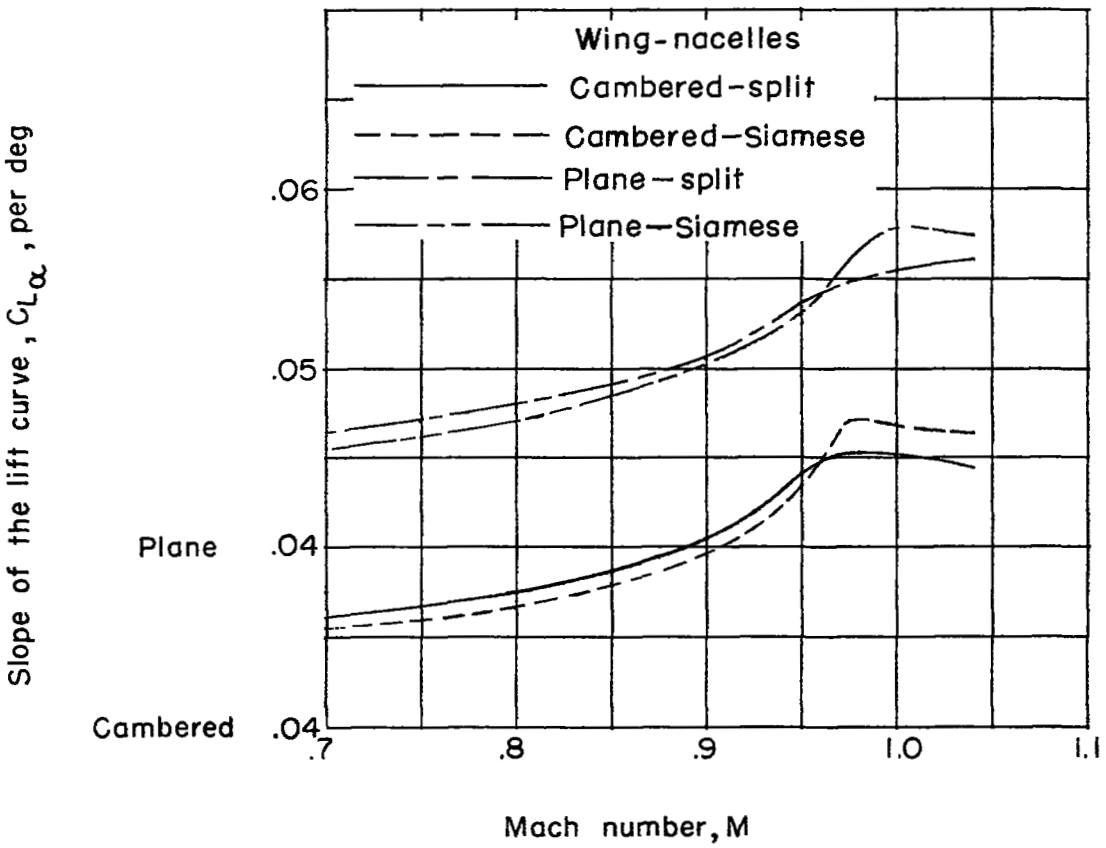

Figure 26.- Variation of the lift-curve slopes with Mach number for the four-engine delta-wing airplane models. $\delta = 0^{\circ}$.

[redacted]

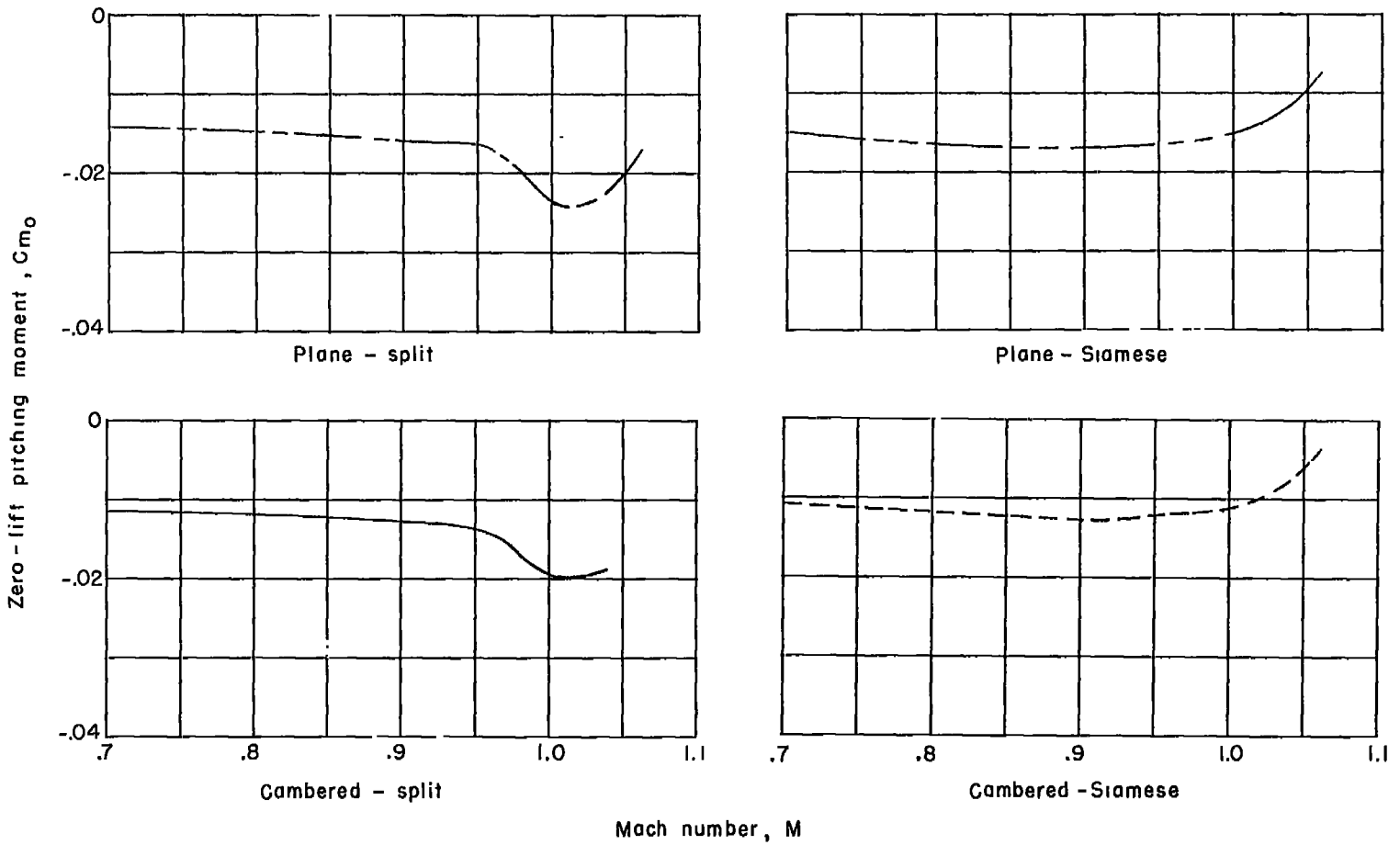

Figure 27.- Effect of Mach number on the zero-lift pitching-moment coefficient for the four-engine delta-wing airplane models. $\delta = 0^{o}$.

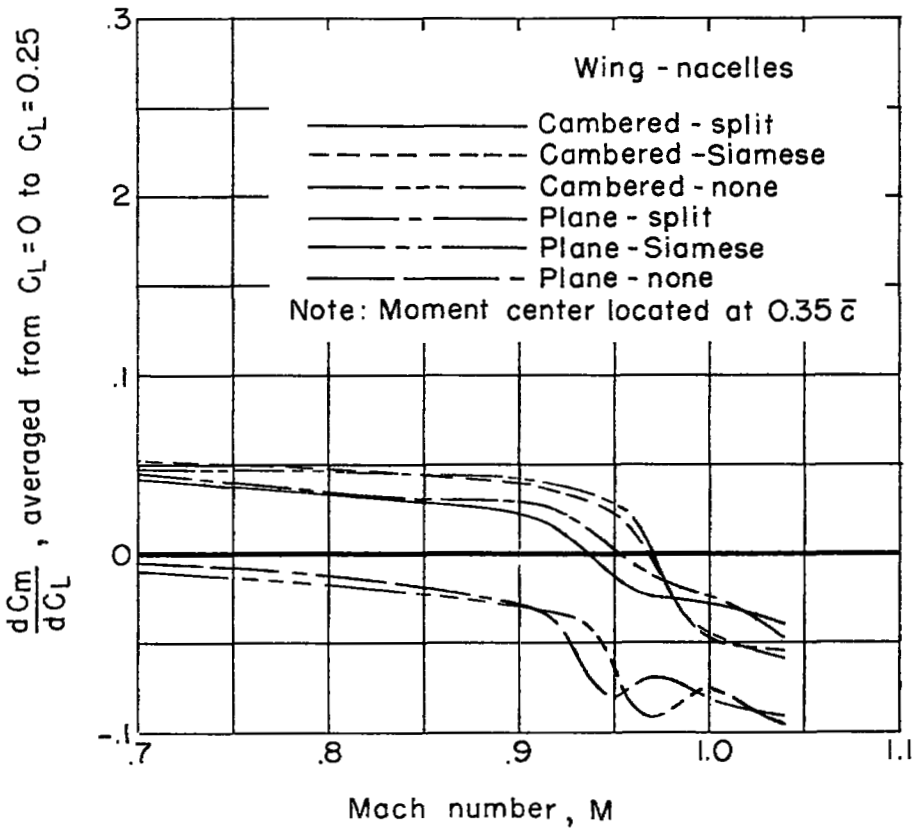

Figure 28.- Effect of Mach number on the slope of pitching-moment coefficient against lift coefficient for the four-engine delta-wing airplane models. $\delta = 0^{\circ}$.

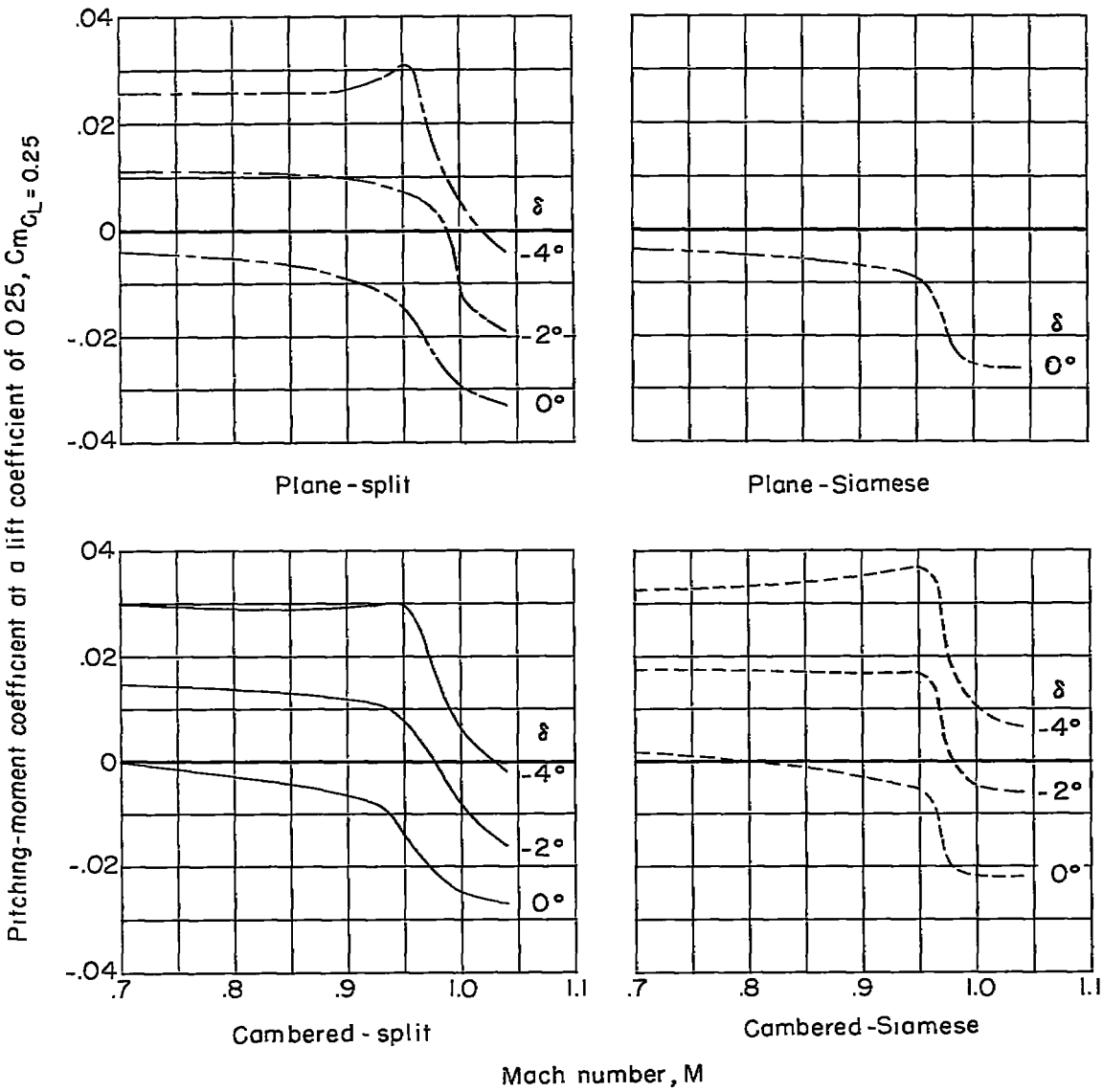

Figure 29.- Effect of Mach number and elevon setting on the pitching-moment coefficient at a lift coefficient of 0.25 for several configurations of the four-engine delta-wing airplane models.

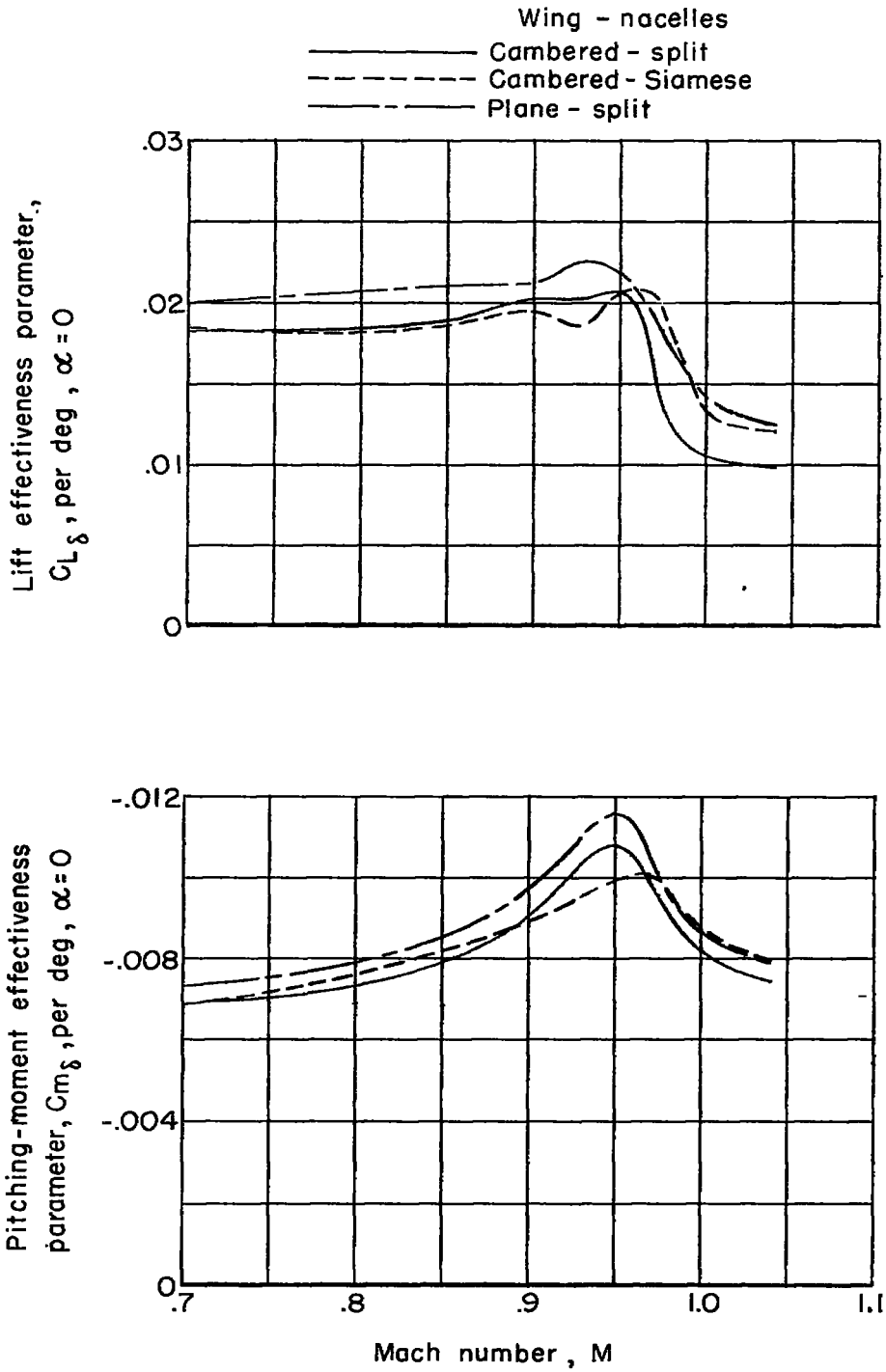

Figure 30.- Variation of elevon effectiveness parameters with Mach number for the four-engine delta-wing airplane models.

[redacted]

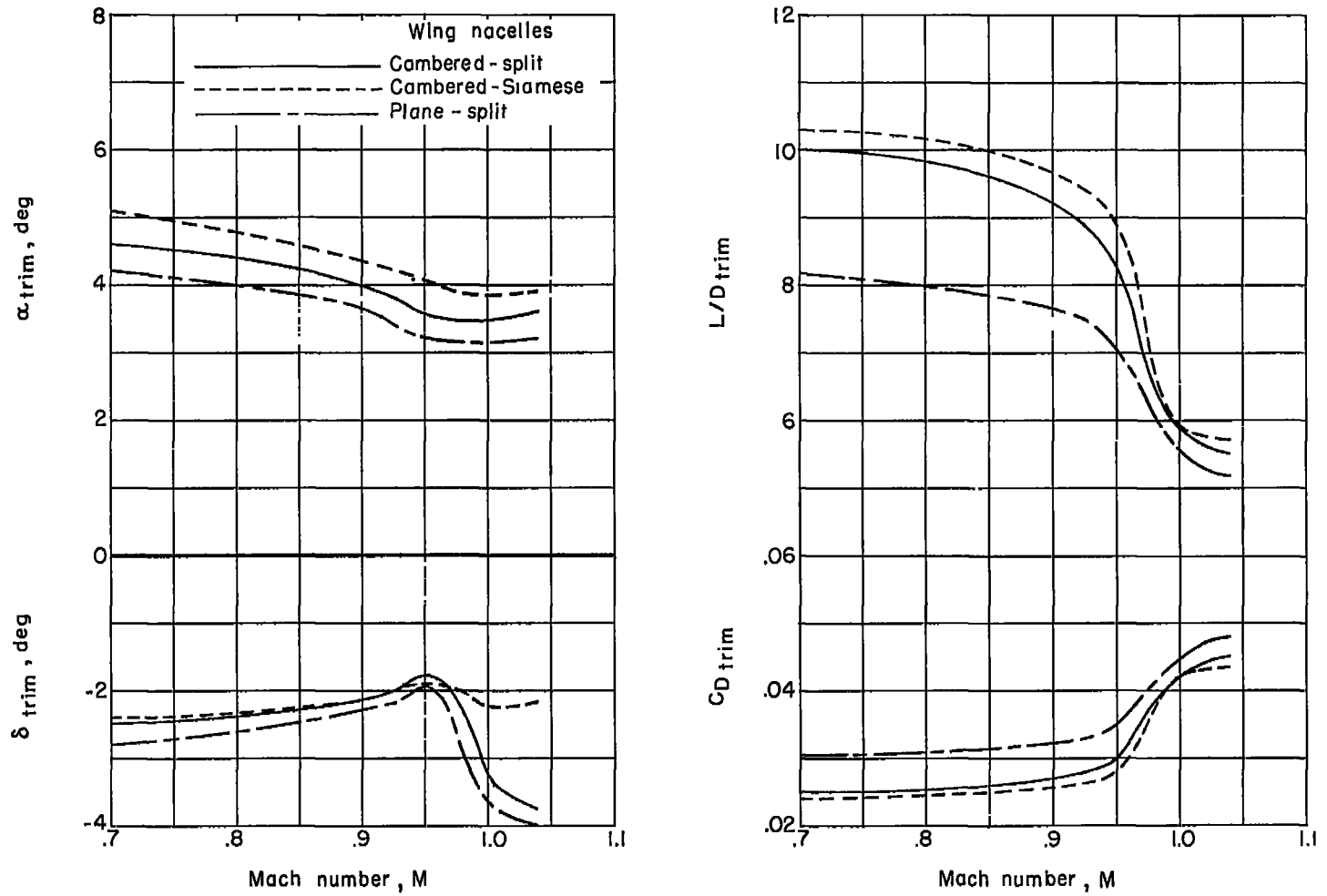

Figure 31.- Variation of elevon angle, angle of attack, drag coefficient, and lift-drag ratio at trim (maintaining a 3-percent static margin and a lift coefficient of 0.25) with Mach number for the four-engine delta-wing airplane models.